Improvement and development of dating methods using radiation damage for reconstructing Quaternary volcanic history

第四紀火山活動史解明のための放射線損傷を利用した
年代測定法の改良と開発

Kentaro ITO

伊藤健太郎

2014年1月

博士論文

Improvement and development of dating methods using radiation damage for reconstructing Quaternary volcanic history

第四紀火山活動史解明のための放射線損傷を利用した
年代測定法の改良と開発

金沢大学大学院自然科学研究科
環境科学専攻
自然計測講座

学　籍　番　号　0823142403
氏　　名　伊藤健太郎
主任指導教員名　長谷部徳子

学 位 論 文 要 旨

博士論文

Improvement and development of dating methods using radiation damage for reconstructing Quaternary volcanic history

第四紀火山活動史解明のための放射線損傷を利用した
年代測定法の改良と開発

金沢大学大学院自然科学研究科
環境科学専攻
自然計測講座

学 籍 番 号　0823142403
氏　　名　伊藤健太郎

Summary

Widespread tephras especially distributed by explosive eruptions are important time markers to correlate the geology of different regions. Several radiometric dating methods have been applied to Quaternary tephras, however each method has its advantages and disadvantages.

In this doctoral thesis, I focused on the potential of fission track dating method using volcanic glass.

I proposed a new method to estimate the track number per unit volume and corresponding age equation. This new dating protocol has the potential to provide reliable fission-track ages without nuclear irradiation and complicated age correction procedures. I constructed an image processing protocol to reduce time-consuming labor works in counting tracks on many screens. This new counting protocol has the potential to provide reliable fission-track ages easily. I also tried to develop a new age determination method in order to offer additional dates for cross-check. I observed young zircons with the atomic force microscope (AFM), and compared to AFM images from old zircon. The cyclic surface structures observed on old zircons were not observed in young zircon, therefore, they may be the results of alpha - recoil tracks which must be in this particular old zircon in the order of 10^{10}/ cm^2.

Abstract

The “Quaternary”, for which the human race becomes adapted to the Earth environment, is the most recent geological period since 2.58 Ma. Among many

environmental factors, a volcanic activity causes damage directly to human beings and volcanic products emitted to the atmosphere would affect the climate (Fig. 1.1). An explosive eruption that largely affects the global environment spreads the volcanic products widely over the world. Widespread tephras especially distributed by explosive eruptions are important time markers to correlate the geology of different regions (e.g. Borchardt et al., 1971; Heiken and Wohletz, 1985; Wicox, 1965). Several radiometric dating methods have been applied to Quaternary tephras. K-Ar method can be applied to several minerals (e.g. feldspars, mica, amphibole or volcanic glass) which are included in tephras (e.g. Bailey et al., 1976; Izett et al., 1970; Izett, 1981; Izett, 1982; Smith, 1979), however, K-rich minerals in tephra sometimes lose radiogenic Ar during secondary hydration and devitrification, which is a specific phenomenon for glass, and hence underestimated ages were reported (Kaneoka, 1972; McDougall and Harrison, 1988). Radiocarbon (^{14}C) method is applicable to inorganic or organic deposits (e.g. Aitken, 1990; Black, 1975; Hildreth, 1981; Miller and Smith, 1987), though materials containing carbon are rarely associated with active lava flows and the technique's dating range is limited to up to around 40,000 years (Fattahi and Stokes, 2003). Luminescence method is also able to apply to several minerals (e.g. feldspar, glass and quartz) in most volcanic products (e.g. Berger, 1992), though problems of the method include such as a type of signal instability called *anomalous fading* of blue luminescence from feldspar (Wintle, 1973; Wintle, 1974); the poor signal-to-noise ratio of quartz and glass thermoluminescence and optically stimulated luminescence analyses (Berger and Huntley, 1994; Miallier et al., 1991). Fission track (FT) dating method has

been often applied to zircon or volcanic glass in Quaternary tephra (e.g., Gentner et al., 1969; Ito and Hasebe, 2011; Naeser et al., 1973; Seward, 1979; Stozer and Wagner, 1969; Walter, 1989; Westgate, 1989). For dating zircon by FT method, a zeta calibration (Hurford and Green, 1982; Hurford and Green, 1983), which needs a neutron irradiation in a reactor, is recommended by the Subcommission on Geochronology (Hurford, 1990). Finding zircons in Quaternary tephra is sometimes difficult due to chemical composition or fractionation in mineral assemblages during the eruption-transportation-occurrence processes. On the other hand, FT method using volcanic glass is applicable to many kinds of tephras because volcanic glass is contained in almost all tephras. However the FT method using volcanic glass needs observation of wide surface area to obtain statistically significant number of tracks because glass contains less uranium compared to zircon or apatite, and target ages is Quaternary, which is relatively short time period to produce tracks in most cases (e.g., Moriwaki et al., 2008; Shane et al., 1995; Walter, 1989). Additionally FT in volcanic glass became reduced in size at ambient temperatures, therefore, several correction procedures were proposed (e.g. Gentner et al., 1969; Stozer and Wagner, 1968; Westgate, 1989). The conventional correction procedure takes a long time (30 - 100 days) and also requires the use of radioactive material produced by thermal neutron irradiation at the nuclear reactor. Thus, each method has its advantages and disadvantages. Therefore multiple analyses by several dating methods are needed to know the history of the volcanic activity for further information.

Recently FT method using volcanic glass has rarely applied to the tephra because of

complicated and time-consuming corrections in spite of a large amount of volcanic glass being contained in the variety of widespread tephra. If volcanic glass is dated, important and rich information will be provided for reconstructing Quaternary volcanic history. Therefore, in this doctoral thesis, I proposed new protocol for FT method using volcanic glass in order to provide reliable data easily, and also tried to develop new age determination method in order to offer additional date for cross-check.

First in chapter 2, I propose a new method to estimate the track number per unit volume and corresponding age equation. The number of tracks per unit volume must be constant provided that complete track fading does not occur. When the track number per unit volume, instead of the track number per unit area, is used in the age equation, there is no need for age correction. Obsidian shards with known induced FT density were etched in a stepwise manner and all induced FTs were observed through the etching of a significant glass volume. The induced FT number per unit volume is calculated from the number of observed tracks and the glass volume removed by the etching, which is estimated on the basis of a track etching model and measurement of track geometry, and then compared with the expected FT density. As a result, bulk etching rate and the track density are obtained, suggesting that this new dating protocol has the potential to provide reliable fission-track ages without nuclear irradiation and complicated age correction procedures. However this new FT counting strategy in volcanic glass results in a further increase in the number of observed screens. Therefore in the chapter 3, I construct an image processing protocol to reduce time-consuming labor works in counting tracks on many screens. I firstly obtained images of spontaneous tracks in

obsidian shards under the microscope. Effects of image capturing conditions on the following image processing are examined. Images must be acquired under some conditions, and the focus must be on the surface within 1 micron above. Image processing detects both of tracks and other structures such as inclusions, dusts, etc. To distinguish ”true” tracks from other structures, circularity and the number of minimum points in the brightness profile along the long axis of ellipse are effective. This new counting protocol has the potential to report more precise fission-track ages without labor works because the image processing can count the number of tracks more than researchers can count. Finally in chapter 4, I also tried to develop a new age dating method in order to cross-check the ages by multiple methods on the same tephra. I observed zircon by the atomic force microscope (AFM) and examined surface regular patterns that were reported by Ohishi and Hasebe (2012). Considering that there might be a possibility that these patterns will be given by alpha recoil tracks, I examined AFM images for these patterns using the zircons from young volcanic rocks in Quaternary (recent rock and 0.32 ± 0.05 Ma) and old zircon (33.0 ± 1.0 Ma) after annealing treatments. The cyclic surface structures with amplitude of 1 - 2 nm was faintly found in the AFM images of young zircons. The small pits, which look like alpha recoil tracks (ARTs) with the depth of 4 - 6 nm, were also observed. Therefore the cyclic surface structures observed on old zircons (waveform with the amplitude of > 4 nm) may be the results of many ARTs formation. The cyclic surface structures are still observed in old zircon after annealing at high temperatures. Hence if these cyclic surface structures are formed by the ARTs, the ARTs might be able to be annealed at more than 1000°C. To

apply ART dating, further understanding on how ART looks like on AFM or other nano-scale imaging must be necessary.

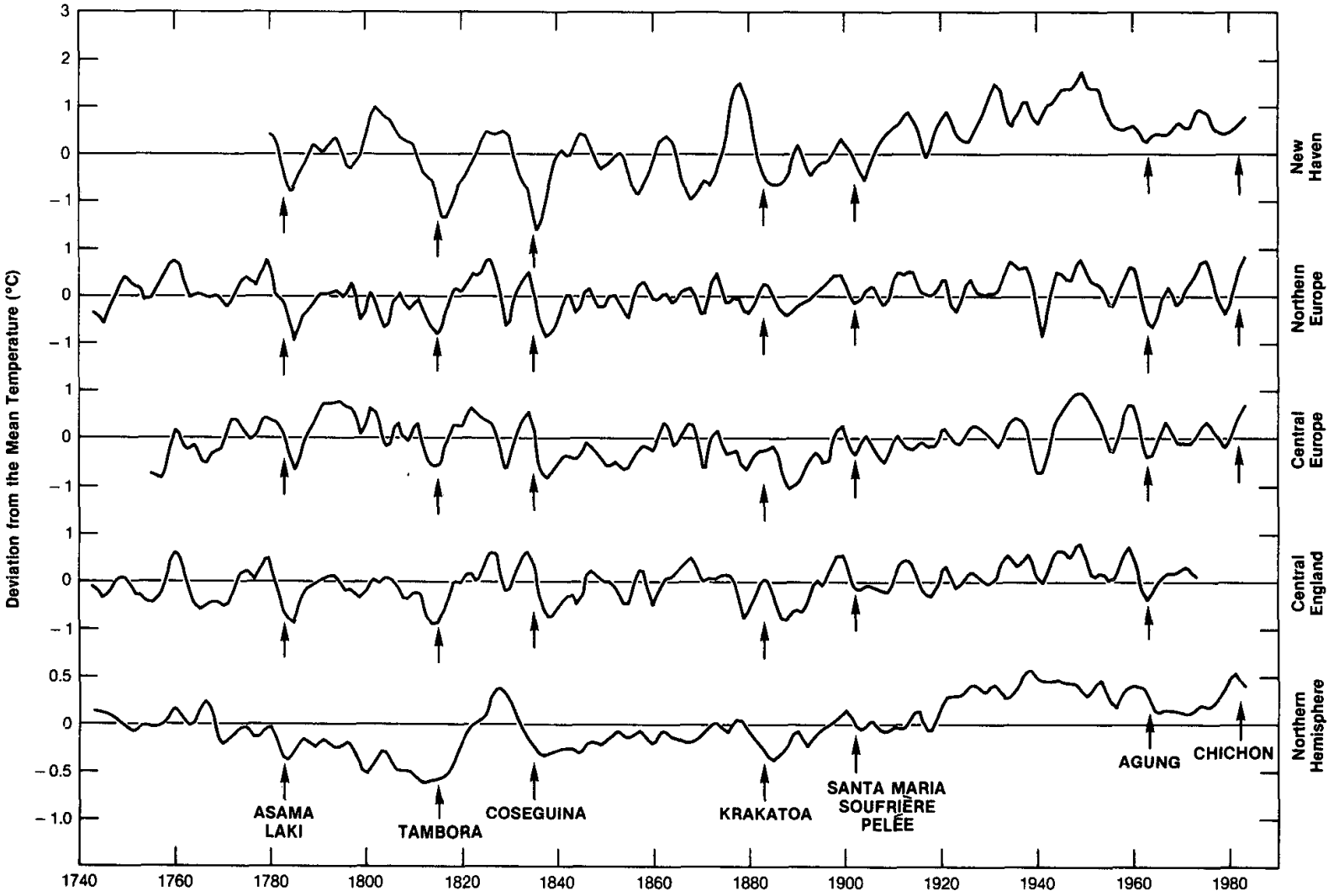

Fig. 1.1

Long-term variation in surface temperature (°C) at New Haven, Connecticut in U.S.A., in Northern Europe, Central Europe, Central England and Northern hemisphere. The arrows show the dates of the volcanic episodes considered in Angell and Korshover, 1985.

Contents

1. Outline of this study

The "Quaternary", for which the human race becomes adapted to the Earth environment, is the most recent geological period since 2.58 Ma. Among many environmental factors, a volcanic activity causes damage directly to human beings and volcanic products emitted to the atmosphere would affect the climate (Fig. 1.1). An explosive eruption that largely affects the global environment spreads the volcanic products widely over the world. Widespread tephras especially distributed by explosive eruptions are important time markers to correlate the geology of different regions (e.g. Borchardt et al., 1971; Heiken and Wohletz, 1985; Wicox, 1965). Several radiometric dating methods have been applied to Quaternary tephras. K-Ar method can be applied to several minerals (e.g. feldspars, mica, amphibole or volcanic glass) which are included in tephras (e.g. Bailey et al., 1976; Izett et al., 1970; Izett, 1981; Izett, 1982; Smith, 1979), however, K-rich minerals in tephra sometimes lose radiogenic Ar during secondary hydration and devitrification, which is a specific phenomenon for glass, and hence underestimated ages were reported (Kaneoka, 1972; McDougall and Harrison, 1988). Radiocarbon (^{14}C) method is applicable to inorganic or organic deposits (e.g. Aitken, 1990; Black, 1975; Hildreth,

1981; Miller and Smith, 1987), though materials containing carbon are rarely associated with active lava flows and the technique's dating range is limited to up to around 40,000 years (Fattahi and Stokes, 2003). Luminescence method is also able to apply to several minerals (e.g. feldspar, glass and quartz) in most volcanic products (e.g. Berger, 1992), though problems of the method include such as a type of signal instability called *anomalous fading* of blue luminescence from feldspar (Wintle, 1973; Wintle, 1974); the poor signal-to-noise ratio of quartz and glass thermoluminescence and optically stimulated luminescence analyses (Berger and Huntley, 1994; Miallier et al., 1991). Fission track (FT) dating method has been often applied to zircon or volcanic glass in Quaternary tephra (e.g., Gentner et al., 1969; Ito and Hasebe, 2011; Naeser et al., 1973; Seward, 1979; Storzer and Wagner, 1968; Walter, 1989; Westgate, 1989). For dating zircon by FT method, a zeta calibration (Hurford and Green, 1982; Hurford and Green, 1983), which needs a neutron irradiation in a reactor, is recommended by the Subcommission on Geochronology (Hurford, 1990). Finding zircons in Quaternary tephra is sometimes difficult due to chemical composition or fractionation in mineral assemblages during the eruption-transportation-occurrence processes. On the other hand, FT method

using volcanic glass is applicable to many kinds of tephras because volcanic glass is contained in almost all tephras. However the FT method using volcanic glass needs observation of wide surface area to obtain statistically significant number of tracks because glass contains less uranium compared to zircon or apatite, and target ages is Quaternary, which is relatively short time period to produce tracks in most cases (e.g., Moriwaki et al., 2008; Shane et al., 1995; Walter, 1989). Additionally FT in volcanic glass became reduced in size at ambient temperatures, therefore, several correction procedures were proposed (e.g. Gentner et al., 1969; Storzer and Wagner, 1968; Westgate, 1989). The conventional correction procedure takes a long time (30 - 100 days) and also requires the use of radioactive material produced by thermal neutron irradiation at the nuclear reactor. Thus, each method has its advantages and disadvantages. Therefore multiple analyses by several dating methods are needed to know the history of the volcanic activity for further information.

Recently FT method using volcanic glass has rarely applied to the tephra because of complicated and time-consuming corrections in spite of a large amount of volcanic glass being contained in the variety of widespread tephra. If volcanic glass is dated, important and rich information will be provided for reconstructing

Quaternary volcanic history. Therefore, in this doctoral thesis, I proposed new protocol for FT method using volcanic glass in order to provide reliable data easily, and also tried to develop new age determination method in order to offer additional date for cross-check.

First in chapter 2, I propose a new method to estimate the track number per unit volume and corresponding age equation. The number of tracks per unit volume must be constant provided that complete track fading does not occur. When the track number per unit volume, instead of the track number per unit area, is used in the age equation, there is no need for age correction. Obsidian shards with known induced FT density were etched in a stepwise manner and all induced FTs were observed through the etching of a significant glass volume. The induced FT number per unit volume is calculated from the number of observed tracks and the glass volume removed by the etching, which is estimated on the basis of a track etching model and measurement of track geometry, and then compared with the expected FT density. As a result, bulk etching rate and the track density are obtained, suggesting that this new dating protocol has the potential to provide reliable fission-track ages without nuclear irradiation and complicated age correction procedures. However this new FT

counting strategy in volcanic glass results in a further increase in the number of observed screens. Therefore in the chapter 3, I construct an image processing protocol to reduce time-consuming labor works in counting tracks on many screens. I firstly obtained images of spontaneous tracks in obsidian shards under the microscope. Effects of image capturing conditions on the following image processing are examined. Images must be acquired under some conditions, and the focus must be on the surface within 1 micron above. Image processing detects both of tracks and other structures such as inclusions, dusts, etc. To distinguish ”true” tracks from other structures, circularity and the number of minimum points in the brightness profile along the long axis of ellipse are effective. This new counting protocol has the potential to report more precise fission-track ages without labor works because the image processing can count the number of tracks more than researchers can count. Finally in chapter 4, I also tried to develop a new age dating method in order to cross-check the ages by multiple methods on the same tephra. I observed zircon by the atomic force microscope (AFM) and examined surface regular patterns that were reported by Ohishi and Hasebe (2012). Considering that there might be a possibility that these patterns will be given by alpha recoil tracks, I

examined AFM images for these patterns using the zircons from young volcanic rocks in Quaternary (recent rock and 0.32 ± 0.05 Ma) and old zircon (33.0 ± 1.0 Ma) after annealing treatments. The cyclic surface structures with amplitude of 1 - 2 nm was faintly found in the AFM images of young zircons. The small pits, which look like alpha recoil tracks (ARTs) with the depth of 4 - 6 nm, were also observed. Therefore the cyclic surface structures observed on old zircons (waveform with the amplitude of > 4 nm) may be the results of many ARTs formation. The cyclic surface structures are still observed in old zircon after annealing at high temperatures. Hence if these cyclic surface structures are formed by the ARTs, the ARTs might be able to be annealed at more than 1000°C. To apply ART dating, further understanding on how ART looks like on AFM or other nano-scale imaging must be necessary.

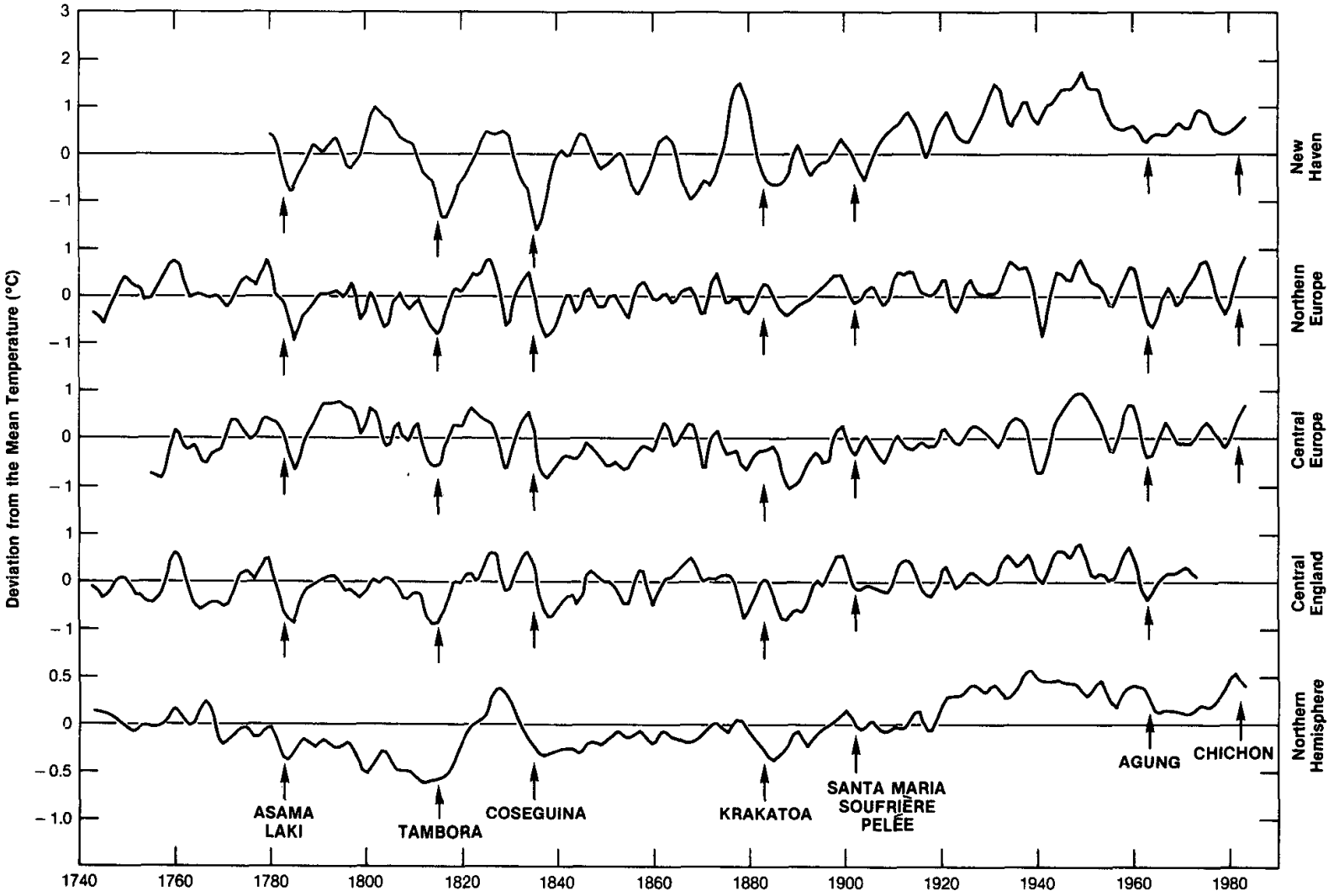

Fig. 1.1

Long-term variation in surface temperature (°C) at New Haven, Connecticut in U.S.A., in Northern Europe, Central Europe, Central England and Northern hemisphere. The arrows show the dates of the volcanic episodes considered in Angell and Korshover, 1985.

Result in this chapter was already published in *Radiation Measurements*.

See the journal home page (http://www.journals.elsevier.com/radiation-measurements).

Chapter 2:

Fission-track dating of Quaternary volcanic glass by stepwise etching

2.1. Introduction

Widespread tephras distributed by explosive eruptions are important time markers for correlating the geology of different regions. Volcanic glass in tephra has a distinctive form, color and refractive index that correspond to a type of eruption and magma chemical composition and are useful for tephra identification (e.g., Borchardt et al., 1971; Heiken and Wohletz, 1985; Wilcox, 1965).

The fission-track (FT) method has been often applied in the age determination of volcanic glass (e.g., Bigazzi et al., 1993; Walter, 1989; Westgate, 1989). FT dating involves counting the tracks left in a material by the spontaneous nuclear fission of ^{238}U. A sample is polished to expose a flat and even surface and then etched chemically to reveal FTs that are visible under an optical microscope. The number of FTs observed on the surface per unit area is used to calculate the age of the material (e.g., Walter, 1989). However, the size of the FTs in volcanic glass is reduced at ambient temperatures. As a result, less FTs intersect the observed surface and the

calculated FT age is younger than the eruption age. To avoid underestimation of the age, several correction procedures have been proposed. Storzer and Wagner (1968) adopted the track diameter as an indicator of the degree of annealing. In this method, the "true" FT density is estimated using the ratio of the mean diameter of spontaneous tracks to that of induced tracks. In the isothermal plateau FT method proposed by Westgate (1989), a sample is irradiated in a nuclear reactor and exposed to a constant temperature (about 100 °C) for about 100 days together with unirradiated glass. The corrected age can be determined from the isothermal plateau ratio of the spontaneous track density to the induced track density plotted against the time. This correction procedure takes a long time (30 - 100 days) and requires the use of radioactive material produced by thermal neutron irradiation at the nuclear reactor.

Although the number of FTs that intersect an observed surface decrease as the FTs become smaller, the number of tracks per unit volume must be constant provided that complete track fading does not occur. When the track number per unit volume, instead of the track number per unit area, is used in the age equation, there is no need for age correction.

This study proposes a new method to estimate the track number per unit volume and an age equation. We etched obsidian shards with known induced FT density in a stepwise manner and observed all induced FTs appearing through the etching of a significant glass volume. The induced FT number per unit volume is calculated from the number of observed tracks and the glass volume removed by the etching, which is estimated on the basis of a track etching model and measurement of track geometry, and then compared with the expected FT density.

2.2. Samples

The obsidian shards used in this study were collected from the chilled margin of Quaternary (0.8 - 0.9 Ma, Kitada et al., 1993; Kitada et al., 1994a) rhyolitic intrusive rock at Wada Pass, Nagano Prefecture, central Japan. The reported spontaneous track density (3030 counts / cm^2, Kitada et al., 1994a) is negligible for the following experiment. Obsidian shards were mounted in epoxy resin (SpeciFix-20) and polished on a grinder using 15 μm and 3 μm diamond pastes. Some mounts were irradiated by thermal neutrons in a nuclear reactor to produce a known number of induced FTs per unit volume for the stepwise etching experiment and others were used for the chemical composition measurement without irradiation.

2.3. Uranium concentration

The uranium concentration was measured by laser ablation inductively coupled plasma mass spectrometry (LA-ICP-MS; Agilent 7500 equipped with a Microlas Excimar laser ablation system, Morishita et al., 2005). Details of the analysis are presented in Table 2.1. SRM 610 and 612 standard glasses, provided by the National Institute of Standards and Technology (NIST), were used as external standards and ^{29}Si as used as an internal standard to convert the signal intensity to a concentration (Pearce et al., 1997; Carpenter and Reimer, 1974; Longerich et al., 1996; Hasebe et al., 2004). The concentration of the internal standard must be known in both the unknown samples and external standard.

To measure the SiO_2 concentration in the glass sample, the chemical composition of the major elements was determined by scanning electron microscope (Akashi α30A) energy dispersive X-ray (SEM-EDX) analysis (Philips EDX9100) with an accelerating voltage of 20 kV (Table 2.2).

The obtained uranium concentration (Table 2.3, 9.05 - 9.29 μg / g) was concordant with the result from neutron activation analysis (Kitada et al., 1994b). Although signals of additional isotopes were acquired in LA-ICP-MS analysis

(Table 2.1), their concentrations are not the main topic of this paper and therefore will be discussed elsewhere.

2.4. Neutron irradiation

The obsidian shards were irradiated at the Thermal Column Pneumatic Tube facility of the Kyoto University Research Reactor (KUR) for 2 h to provide a known induced track density for the stepwise etching experiment.

The induced track number per unit volume (N_i) was calculated using (Wagner and Van den haute, 1992)

$$N_i = {}^{238}N I \sigma \phi \qquad (1)$$

where ${}^{238}N$ is the number of ${}^{238}U$ per unit volume, I is the isotopic ratio of ${}^{235}U$ / ${}^{238}U$ (1/137.88; Cowan and Adler, 1976), σ is the cross section of the neutron-induced fission of ${}^{235}U$ (5.80×10^{-22} cm^2; Hanna et al., 1969), and ϕ is the thermal neutron dose (2.8×10^{15} cm^{-2}), which is estimated from the neutron flux published by KUR (4×10^{11} cm^{-2}s^{-1}) and may have an error of - 15% because of statistical variation in the nuclear reaction or sample spacing within the irradiation facility.

$$^{238}N = {}^{238}U \cdot 10^{-6} \cdot \left(\frac{N_A}{M} \right) \cdot d\,, \qquad (2)$$

where ${}^{238}U$ is the concentration of ${}^{238}U$ obtained from the LA-ICP- MS results (9.19

± 0.04 mg / g), N_A is Avogadro's number (6.02×10^{23}), M is the mass number of ^{238}U (238), and d is the obsidian density (2.43 ± 0.09 g / cm^3). As a result, $^{238}N = 5.6 \pm 0.2$ ($\times 10^{16}$ cm^{-3}) and $N_i = 6.8 \pm 1.1$ ($\times 10^8$ cm^{-3}) for the sample.

2.5. Stepwise etching

Glass samples with known induced FT density were etched in 24% or 12% hydrofluoric acid (HF) at 30 °C (Miller and Wagner, 1981; Wagner, 1976; Walder and Mark, 1988; Westgate, 1989) for 15 or 90 s respectively. These two samples were then observed under an optical microscope (Eclipse E600, Nikon) and photographs of four 100 μm × 100 μm screens were taken of each mount to count the number of tracks and measure the track diameters. Afterwards, the samples were etched again for 15 s (24% HF) or 90 s (12% HF) and the same screens were observed. This process was repeated and thus the samples were etched in a stepwise manner. Fig. 2.1 shows examples of photos taken through stepwise etching. Fig. 2.2 shows the accumulated number of surface tracks increases with the etching time for both the mount etched with 12% HF and that etched with 24% HF. The track diameters measured along both the short and long axes are shown in the upper plots of Fig. 2.3.

2.6. Estimation of the bulk etching rate (V_{eg})

To estimate the glass volume observed in extracting tracks, the bulk etching rate (V_{eg}) was estimated using a track etching model and measurements of the track geometry. To examine the reliability of this estimation, the thickness of a sample removed through etching was measured using a micrometer (V_{mg}) and then compared with the thickness estimated.

2.6.1. Direct measurement

The change in the mount thickness before and after etching was measured using a micrometer with precision of ± 0.01 mm (Table 2.4). Four samples were prepared and their thicknesses measured. They were then etched at 30°C: Two mounts were etched for 2 h in 12% HF and the other two for 30 min in 24% HF. Thicknesses after etching were measured. The averages of six measurements before and after etching were used to calculate the etching rate (V_{mg}). V_{mg} values for the two mounts etched with 12% HF were 0.012 ± 0.001 and 0.010 ± 0.0002 μm s^{-1}, and values for the two mounts etched with 24% HF were 0.034 ± 0.002 and 0.037 ± 0.003 μm s^{-1} (where the error is the average standard error).

2.6.2. Estimation based on the track geometry

The model used here to explain the growth of the track geometry through etching was proposed by Ali and Durrani (1977) under the assumption of an isotropic etching rate for the glass (Fig. 2.4). A track that intersects an etched surface is cone-shaped because of the difference between the bulk etching rate and the along-track etching rate; this is referred to the cone phase. As etching proceeds, the part damaged by the track is removed completely, but the morphology of the surface still indicates the existence of the track (transition and sphere phases). Using this model, we estimated the bulk etching rate from the radius growth of tracks that vertically intersect the observed surface. The track geometry was observed under a laser microscope (VK-8550, KEYENCE) at the Central Research Institute of Electric Power Industry (CRIEPI). Fig. 2.5 shows the vertical cross section of a track etched with 12% HF, demonstrating that the observed tracks are in the sphere phase shown in Fig. 2.4. In the sphere phase, the depth of the track is ideally constant as the etching proceeds because the thicknesses of material removed by etching at the bottom of a track and the glass surface are concordant and determined by the bulk etching rate. Table 2.5 gives the results of the track depth measurement of about 20 tracks whose orientations are almost perpendicular to the observed surface. The

average depths are 5.93 ± 0.3 μm for 12% HF and 6.27 ± 0.4 μm for 24% HF etching, which are equivalent within the error range. Therefore, the overall average is calculated to represent the depth of the tracks (6.10 ± 0.25 μm).

The track geometry in this phase is a part of a sphere, and we can therefore express the track radius of an observed etch pit as (Fig. 2.6)

$$R_k = \sqrt{b(2L - b)}, \qquad (3)$$

where R_k is the track radius of the observed (circular) etch pit after k etchings, b is the average track depth (6.10 ± 0.25 μm from observation), and L is the radius of a hypothetical sphere. After $k + 1$ etching cycles,

$$R_{k+1} = \sqrt{b\left\{2\left(L + V_{eg} \cdot t\right) - b\right\}}, \qquad (4)$$

where V_{eg} is the bulk etching rate and t is the unit etching time (in this study, 90 s for 12% HF and 15 s for 24% HF etching). From Eqs. (3) and (4), the following equation is obtained without unknown factor L.

$$V_{eg} = \frac{R_{k+1}^2 - R_k^2}{2bt} \qquad (5)$$

The growth of R and R^2 through etching is shown in Fig. 2.3. Although we attempted to choose tracks perpendicular to the observed surface to obtain circular etch pits, most pits were elliptical. Hence both the major (long) and minor (short)

axes were measured. V_{eg} is calculated (Table 2.6) using the values obtained at the later stage (810 - 1170 s for 12% HF and 135 - 195 s for 24% HF) of stepwise etching experiments, and thus, a track should be in the sphere phase and the *time*-R^2 relationship should be linear (Fig. 2.3). Some of the tracks have a steeper slope in the R^2 graph of longer axes, corresponding to a higher etching rate. The longer axis in many cases corresponds to the direction that a fission fragment traveled; therefore, these tracks may not be in a sphere phase yet. Hence, the shorter axis may be more suitable for the estimation of the bulk etching rate.

2.6.3. Comparison of V_{eg} and V_{mg}

The bulk etching rates are estimated from the etch pit geometry (V_{eg}) and direct measurement (V_{mg}). They agree within the range of error (Fig. 2.7), suggesting that measurement of the track radius growth provides a reasonable estimate of the bulk etching rate. To obtain V_{mg}, very severe etching was necessary to detect a difference in sample thickness before and after etching. Such heavy etching is possible only for samples with significant sizes and may not be applicable to any kind of volcanic glass. Therefore, V_{eg}, which is obtained along with the increase in number of FTs

through the stepwise etching experiment, is hereafter referred to as the bulk etching rate.

2.7. Track number per unit volume

The track number per unit volume (N_e) is calculated from the bulk etching rate V_{eg} (cm / s), the observed area A ($100 \pm 5 \times 100 \pm 5 \times 10^{-4}$ cm^2 in this study) and the rate of the track increase V_{track} (counts / s):

$$N_e = \frac{V_{track}}{V_{eg} A} \qquad (6)$$

V_{track} is estimated from the average slope in Fig. 2.2 and is 0.026 ± 0.002 (count / s) for 12% HF and 0.15 ± 0.02 (count / s) for 24% HF etching. The intercept in Fig. 2.2 (time is 0 s) is hypothetical number of tracks per unit area (a conventional track density) when no bulk etching occurs. FTs found on the surface must come from a significant volume above and below the surface depending on track registration distances within a glass.

From the obtained bulk etching rates (0.010 ± 0.001 and 0.043 ± 0.006 mm s^{-1} for 12% and 24% HF etchants respectively), N_e is estimated to be 2.6 ± 1.7 ($\times 10^8$ counts cm^{-3}) and 3.4 ± 1.3 ($\times 10^8$ counts cm^{-3}) respectively.

Fig. 2.8 compares the expected track density N_i and observed track density N_e. The error ranges are large for both and the estimated N_e is less than the expected N_i. However, when the two-sigma error range is considered, the values agree. We estimated N_i on the basis of published thermal neutron flux; nonetheless, it must be difficult to obtain the correct value. Our long-term monitoring of flux through the irradiation of standard glass, which is necessary for conventional zeta calibration in FT dating, suggests that the neutron flux varies by more than 50% over time. This leads us to believe that the estimated value reasonably matches the expected value and suggests that the proposed protocol can provide a reliable estimation of the track number per unit volume.

2.8. Age equation

In this section, an age equation that includes the analytical values proposed here is presented. The general age equation for FT dating is

$$t = \frac{1}{\lambda_\alpha} \ln\left(\frac{\lambda_\alpha}{\lambda_f} \frac{N_s}{^{238}N} + 1 \right) \qquad (7)$$

where N_s is the number of spontaneous tracks per unit volume and ^{238}N is the number of ^{238}U atoms per unit volume. The number of ^{238}U (i.e., ^{238}N) is calculated using ^{238}U concentrations (μg / g) obtained from LA-ICP-MS analysis and Eq. (2).

Consequently, an age equation can be derived by substituting Eqs. (2) and (6) into Eq. (7):

$$t = \frac{1}{\lambda_\alpha} \ln\left\{ \frac{\lambda_\alpha}{\lambda_f} \left(\frac{\frac{V_{track}}{V_{eg}} \times 10^8}{^{238}U \times 10^{-6} \times \frac{N_A}{M} \times d} \right) + 1 \right\} \qquad (8)$$

$$t = \frac{1}{\lambda_\alpha} \ln\left\{ \frac{\lambda_\alpha}{\lambda_f} \frac{V_{track} M}{\left(V_{eg} \cdot {}^{238}U \cdot N_A \cdot d \right)} \times 10^{14} + 1 \right\}$$

2.9. Conclusion

This study proposes a new dating protocol for volcanic glass that estimates the uranium concentration in LA-ICP-MS analyses and the track number per unit volume from observations of the number of tracks and track geometry in stepwise etching. The bulk etching rate was successfully estimated on the basis of geometry change, having a value concordant with the measured etching rate. The rate of increase in the number of tracks in stepwise etching, combined with the bulk etching rate, allows the estimation of the track number per unit volume and can be used in the age equation along with the uranium concentration measured by LA-ICP-MS. This method may not be useful for samples with high track density for which overlap of tracks makes identification of each track difficult. With a view to make

this method more practical, an automated track recognition system would be a powerful tool to observe an increase in the number of tracks in stepwise etching.

Table 2.1
Detail of LA-ICP-MS analytical setting.

ICP-MS	
Model	Agilent 7500 s
Forward power	1200 W
Reflected power	1 W
Carrier gas flow	1.2 L min^{-1} (Ar)
	0.3 L min^{-1} (He)
Auxiliary gas flow	1.0 L min^{-1}
Plasma gas flow	15 L min^{-1}
Cones	Pt (sampler and skimmer)
Laser ablation system	
Model	GeoLas Q + (MicroLas)
Wavelength	193nm (Excimer ArF)
Repetition frequency	5 Hz
Energy density at target	8 J cm^{-2}
Spot diameter	40 μm
Background time	25 sec.
Ablation time	25 sec.
Measured mass number	7, 29, 85, 88, 89, 90, 93,133, 138, 139, 140, 146, 147, 151, 158, 163, 166, 172, 175, 178, 208, 232, 238

Table 2.3
^{238}U concentration measured by LA-ICP-MS .

	^{238}U (ppm)
1	9.22
2	9.05
3	9.15
4	9.23
5	9.29
Average	9.19
Standard error	0.04

Table 2.2
Chemical composition of major elements (wt%) measured by SEM-EDX.

	SiO_2	TiO_2	Al_2O_3	Cr_2O_3	FeO	MnO	MgO	CaO	Na_2O	K_2O	P_2O_5	NiO	Total
1	76.25	0.14	13.09	0.07	0.60	0.11	0.00	0.47	3.68	4.86	0.08	0.00	99.36
2	76.22	0.10	13.03	0.12	0.66	0.13	0.00	0.35	3.56	4.81	0.23	0.00	99.21
3	77.09	0.03	13.07	0.12	0.60	0.17	0.00	0.40	3.63	4.85	0.07	0.04	100.07
4	75.59	0.15	12.77	0.06	0.61	0.13	0.00	0.42	3.74	4.68	0.03	0.03	98.22
Average	76.29	0.11	12.99	0.09	0.62	0.14	0.00	0.41	3.65	4.80	0.10	0.02	99.22
Standard error	0.53	0.05	0.13	0.03	0.02	0.02	0.00	0.04	0.07	0.07	0.08	0.02	0.66

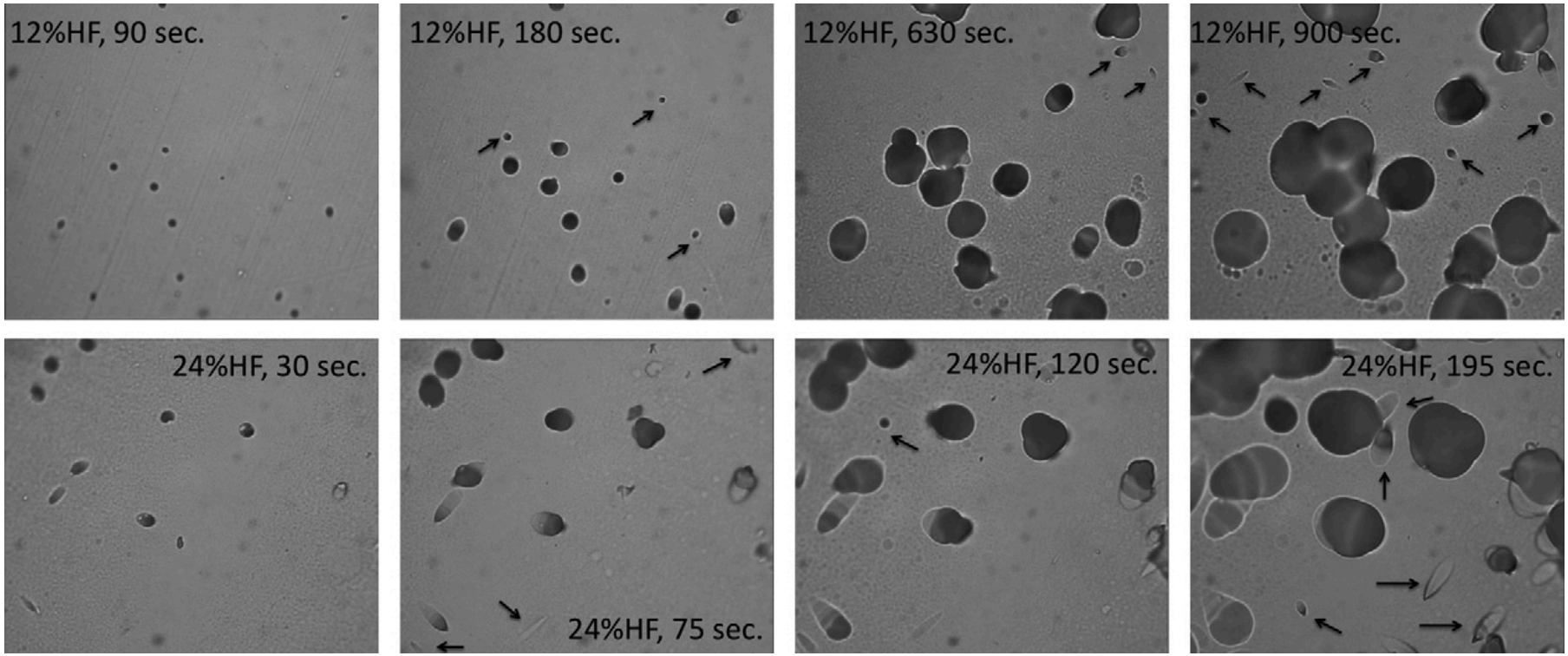

Fig. 2.1
Examples of photos taken during the step-etch experiment. Horizontal width of each image is 35 mm. Arrows indicate tracks that were invisible in the earlier etching stages.

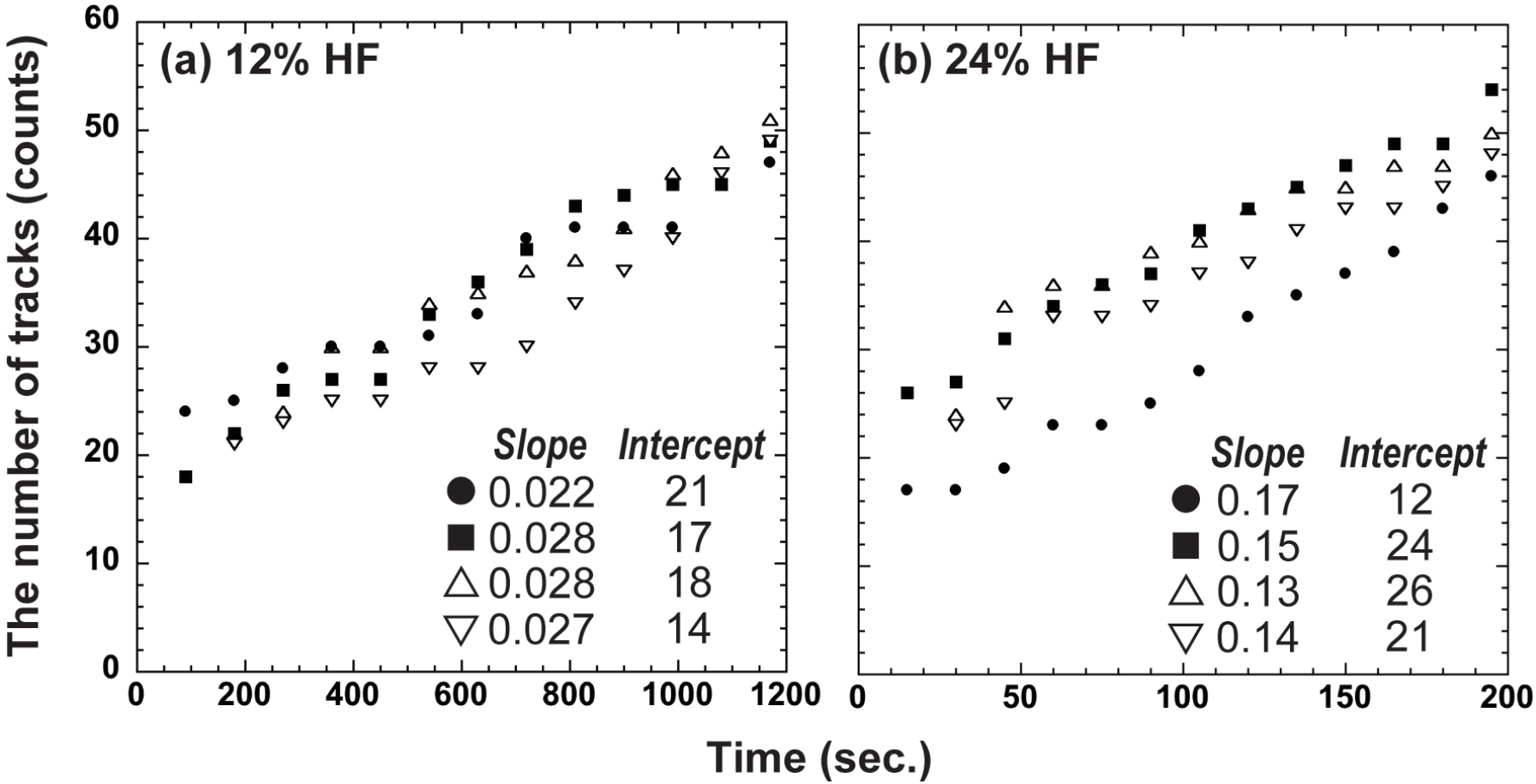

Fig. 2.2

Increase in the accumulated number of surface tracks plotted against etching time. Each marker corresponds to an observed screen (100 μm × 100 μm). The linear fitting line is calculated for each screen and its slope (counts s^{-1}) and intercept (counts) are given. (a) Data for a sample etched with 12% HF. (b) Data for a sample etched with 24% HF.

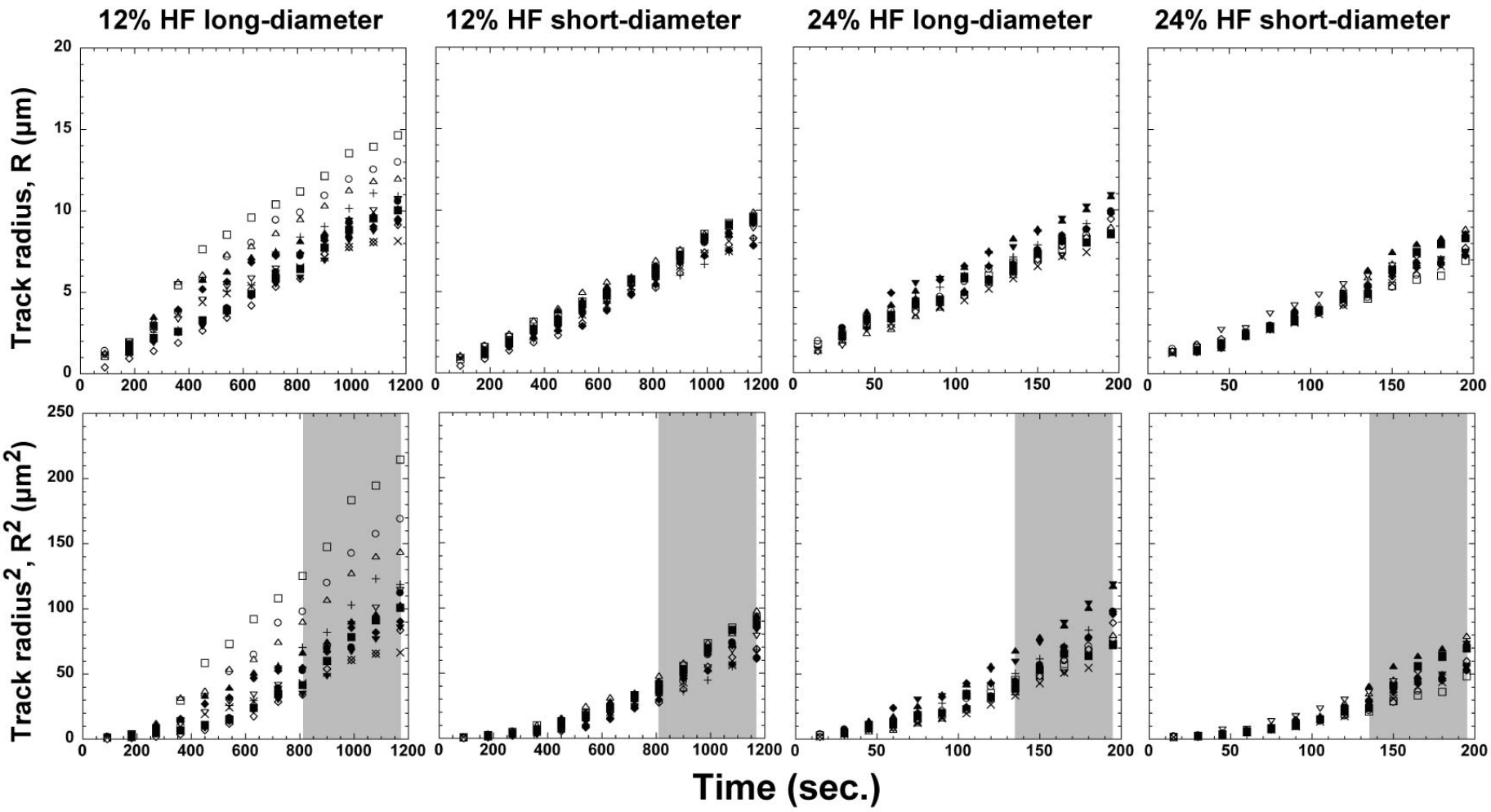

Fig. 2.3

Increase in the track radius (R) measured along the short and long axes plotted against etching time for 12% and 24% HF etchant. Each marker corresponds to a track. R^2 is also calculated and plotted (see Section 2.6.2).

Table 2.4

Measurements of sample thickness before and after massive etching and the bulk etching rate (V_{mg}).

		1st.	2nd.	3rd.	4th	5th	6th	Average	Standard error	V_{mg} (μm s^{-1})	Error
(A) 12% HF											
Sample 1	before(mm)	1.20	1.22	1.22	1.20	1.22	1.19	1.21	0.005	0.012	0.001
	after(mm)	1.05	1.01	1.00	1.02	1.06	1.05	1.03	0.009		
Sample 2	before(mm)	1.46	1.47	1.46	1.46	1.46	1.46	1.46	0.002	0.010	0.0002
	after(mm)	1.33	1.32	1.32	1.32	1.32	1.32	1.32	0.002		
(B) 24% HF											
Sample 3	before(mm)	1.95	1.96	1.96	1.96	1.95	1.95	1.96	0.002	0.033	0.002
	after(mm)	1.85	1.83	1.83	1.84	1.82	1.84	1.84	0.004		
Sample 4	before(mm)	1.18	1.18	1.16	1.18	1.19	1.16	1.18	0.005	0.037	0.003
	after(mm)	1.06	1.01	1.04	1.05	1.05	1.04	1.04	0.006		

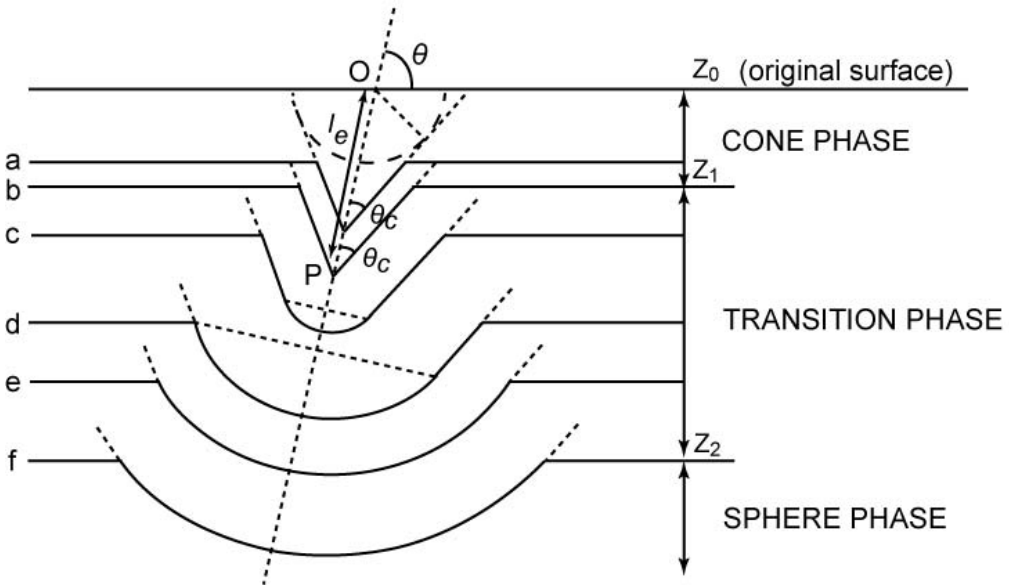

Fig. 2.4

Three phases in the evolution of the shape of an etched track in glass with prolonged etching (from Wagner and Van den haute, 1992. See also Ali and Durrani, 1977). See Wagner and Van den haute (1992) for a detailed explanation.

Table 2.5
Result of track depth measurement.

Track ID	Depth (μm)	
	12% HF	**24% HF**
1	4.20	6.87
2	4.18	7.09
3	6.02	4.66
4	5.71	4.54
5	4.50	8.85
6	4.49	9.10
7	5.11	2.65
8	5.17	3.57
9	6.86	3.31
10	7.82	7.11
11	4.49	7.22
12	4.72	5.91
13	4.94	5.58
14	5.16	6.10
15	6.26	7.43
16	6.02	7.61
17	6.15	6.44
18	6.20	6.74
19	8.88	8.61
20	8.97	8.72
21	8.70	4.91
22	-	4.91
Average	5.93	6.27
Standard error	0.3	0.4
Overall average	6.10	
Standard error	0.25	

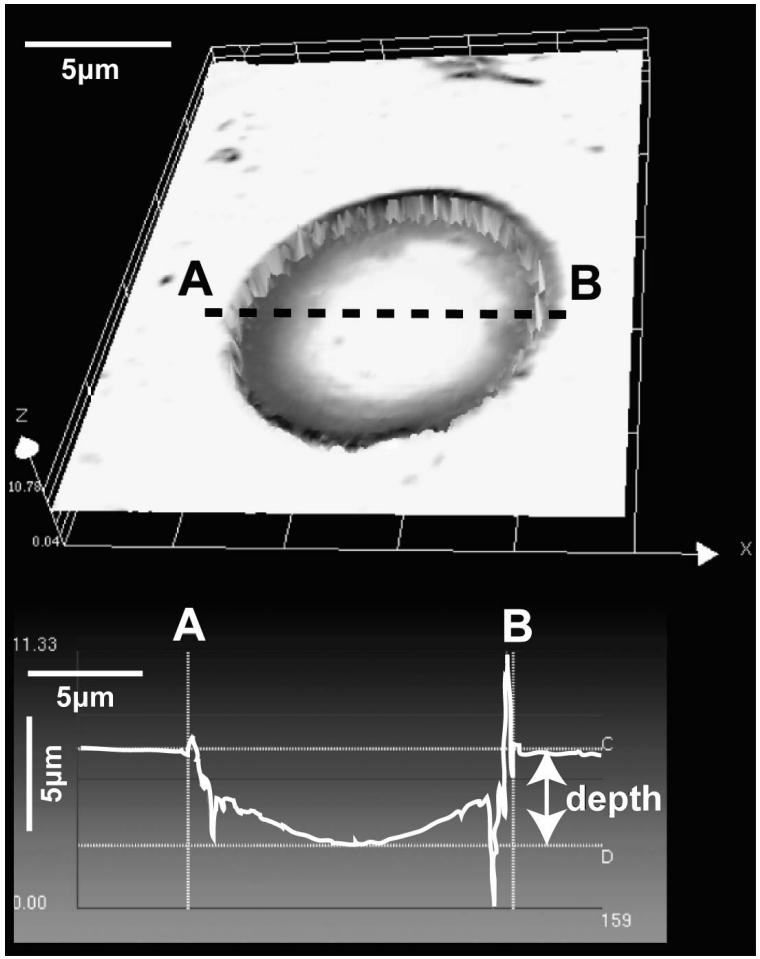

Fig. 2.5
The upper figure shows a three-dimensional image of a track observed under a laser microscope. The cross section along the A-B line is shown in the lower figure.

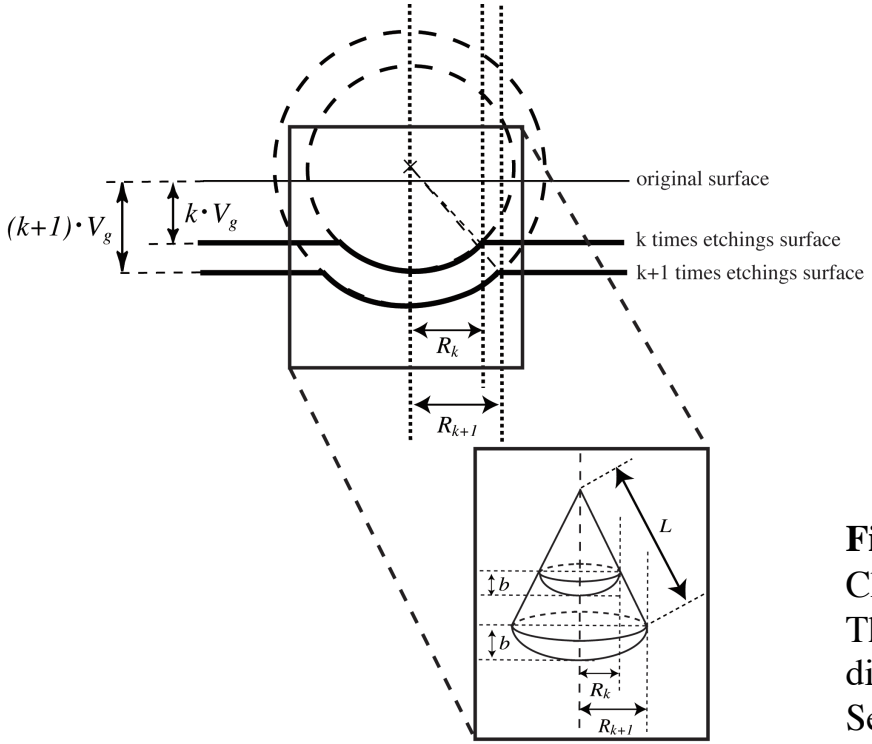

Fig. 2.6
Change in track geometry through progressive etching. The figure shows the cross section of a track with three-dimensional track growth shown in the inserted figure. See the text for a detailed explanation.

Table 2.6
Bulk etching rate (V_{eg}) calculated from the track geometry.

Etchant	Diameter width	V_{eg} (μm s^{-1})	Error[a]	Average	Error
12% HF	long axis	0.01	0.002	0.01	0.002
	short axis	0.010	0.001		
24% HF	long axis	0.06	0.008	0.05	0.007
	short axis	0.04	0.006		

[a] Error is calculated from the standard errors of the R^2 slope (Fig. 2.2) and track depth (Table 2.5).

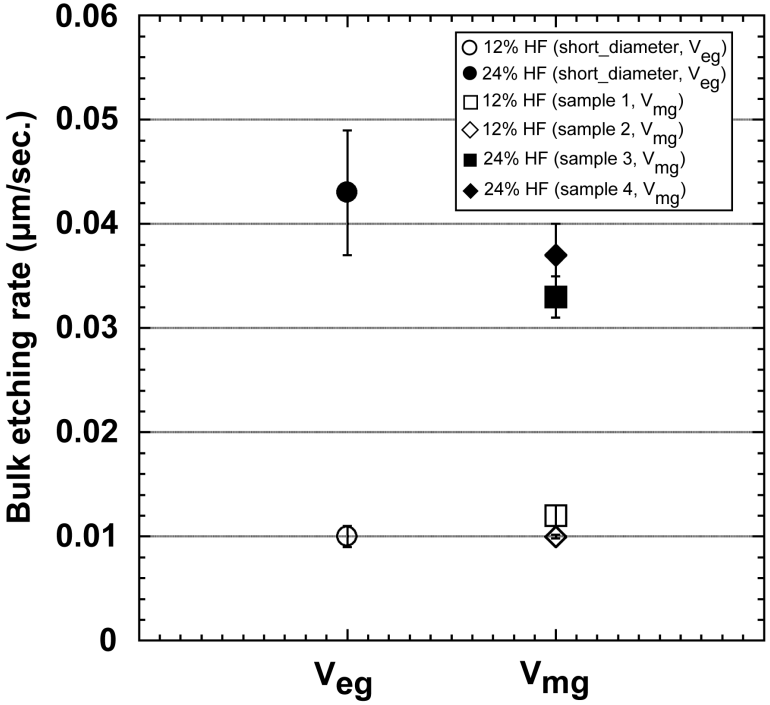

Fig. 2.7
Comparison of bulk etching rates estimated using the etching model and the change in the track radius in progressive etching (V_{eg}) and that measured using a micrometer (V_{mg}). Error bars represent ±σ.

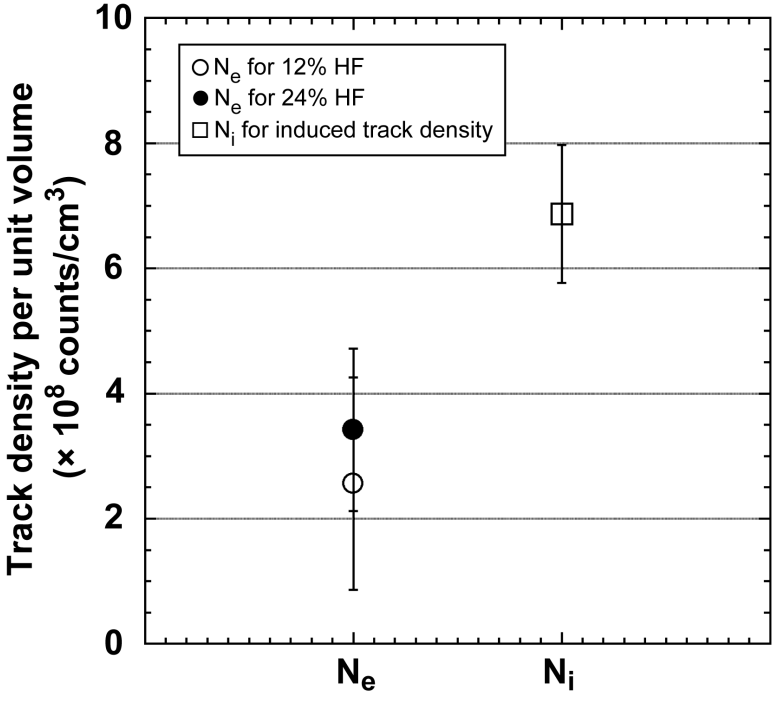

Fig. 2.8
Comparison of the track number per unit volume estimated in the stepwise etching experiment (N_e) and the value expected from nuclear reaction in the reactor (N_i). Error bars represent ±σ.

Chapter 3:

Fission tracks counting in volcanic glass using image-processing

3.1 Introduction

Widespread tephras distributed by explosive eruptions are important time markers to correlate the geology of different regions. (e.g. Borchardt et al., 1971; Heiken and Wohletz, 1985; Wicox, 1965). For age determination of volcanic glass, fission track (FT) method has been often applied (e.g., Gentner et al., 1969; Ito and Hasebe, 2011; Storzer and Wagner, 1968; Westgate, 1989; Walter, 1989). FT method for volcanic glass needs observation of wide area of surface to obtain statistically significant number of tracks counting because glass contains less uranium compared to zircon or apatite, and target ages is Quaternary, which is relatively short time period to produce tracks in most cases (e.g., Moriwaki et al., 2008; Shane et al., 1995; Walter, 1989). FT in volcanic glass became reduced in size at ambient temperatures, therefore, several correction procedures were proposed (e.g. Gentner et al., 1969; Ito and Hasebe, 2011; Storzer and Wagner, 1968; Westgate, 1989). Appling these procedures results in a further increase in the number of

observed screens.

In this work, we try image processing to reduce time-consuming labor works in counting tracks on many screens. We firstly obtained images of spontaneous tracks in obsidian shards under the microscope. Effects of image capturing conditions on the following image processing are examined. To distinguish tracks from noises in the image, we especially focused on circularity and a brightness gradation in detected tracks.

3.2 Experiments

3.2.1. Sample and preparation

The obsidian shards, which were collected from the chilled margin of Quaternary rhyolitic intrusive rock from Wada Pass in Nagano Prefecture, Japan, and were once recommended as the candidate of age standards (Kitada et al., 1994a; Kitada et al., 1994b, JAS-G1), are analyzed.

These shards of ~two centimeter in size were mounted in epoxy resin (SpeciFix-20), and polished with 15μm (polish times is about 5 minutes), 3μm (about 10 minutes) and 1μm (about 30 minutes) diamond paste.

The mounts with obsidian were etched in 24% HF (hydrogen fluoride) at 30°C

(Miller and Wagner, 1981; Wagner, 1976; Walder and Mark, 1988; Westgate, 1989) for 60 sec. After etching, we counted the number of tracks under microscope to compare this counted number with the result from following image processing.

3.2.2. Image capturing conditions: Microscope and camera setting

We considered three types of microscope setting (magnification of objective lens, the brightness and focus, Table 3.1) to discuss the best image capturing conditions for the following image processing to detect tracks. The microscope used to observe tracks is ECLIPSE 80i with transmitted light equipped with the eyepiece of x10 and object lens either x40 or x100. The images were captured by the camera Focus Studio 2100 (Nakaden) with the effective pixels being two million (1,600 × 1,200). The sizes of tracks are approximately from 80 to 200 pixels in the image captured with x40 objective and from 500 to 1200 pixels with x100 objective.

The light source of microscope is a halogen lamp (12V100W) and we tested five steps of the brightness from 0.15 to 4.10 klux (see Table 3.1). We also examined three types of focus. After the focus was set on the surface, sample stage was moved downward or upward by two μm and three images with different focus ("on the surface", "above the surface" or "on the internal surface") were obtained. In total, we

took FT photos under 15 conditions. The tracks in glass normally look like a dark hole with a shape of circular or oval in the images. The glass often contains needle-like crystallites and small gas bubbles which, after etching, are easily confused with tracks.

3.2.3. Image processing

The obtained image was processed to make tracks visible clearly. First we create binary images to distinguish background and structures, which may include tracks and confusing inclusions. Then several image processing are performed to eliminate the noises.

We used OpenCV (Open Source Computer Vision Library) for image processing. OpenCV is an open source library for computer vision and machine learning software. It has C++, C, Python and Java interfaces and supports Windows, Linux, Android and Mac OS X. OpenCV is chosen for image processing in this study because of its multi-platform accessibility and variety of algorithms.

3.2.3.1. Detection of structures on the binary images

We converted captured images into binary images to detect tracks by the following procedures, though the detected structures may include noises (i.e.,

inclusions, scratches, and dust). We firstly ran a conversion into a grey scale images (Fig.3.1a) and subsequently ran a smoothing to avoid the effect of small random noises in the images. Next we carried out an edge detection to find FTs contour and finally got the binary images.

When a noise happens randomly on the image, it causes a significant difference in the brightness between the noise pixels and surrounding pixels. The smoothing processing aims to eliminate noises based on this brightness difference. In this paper, we applied Gaussian smoothing filter to eliminate noises (Fig.3.1b). This Gaussian filter puts the weight on the nearer pixels of the target pixel than the farther pixels in calculating the average brightness of the target pixel. The average was calculated for surrounding 5 × 5 pixels which is small enough to compare the minimum size of tracks being about 80 pixels in the x40 image.

Then, the edges of the structures (tracks) were detected by the Laplacian filter. A boundary of an object shows an abrupt change in the brightness, which form a contour. The Laplacian filter calculates the second-order differential to detect the abrupt change in the brightness. The calculation was applied to 5 × 5 pixels around the target, because the small noises less than 5 × 5 pixels were already eliminated by

the preceding Gaussian filtering. After the Laplacian filter, images show the edge of the structures (Fig.3.1c).

Finally we converted the grey scale image, which is already done the smoothing and the edge detection processings, into a binary image in order to distinguish structures (FTs) from the background (Fig.3.1d). The binarization converts pixels below the threshold into black (0) or pixels above the threshold into white (255). To determine the threshold, we applied Otsu's method (Otsu, 1979) which automatically performs clustering-based image thresholding. The algorithm assumes that the image contains two classes of pixels (bi-modal in brightness histogram), and then finds the optimum threshold in separating those two classes by calculating the variance of each class and making the sum of the variances minimal.

On this binary image, structures are detected by the algorithm developed by Suzuki and Abe (1985), which is implemented as one of the functions in OpenCV. This algorithm detects the borders in a binary image and determines the enclosing relationships among these borderlines. A border is detected as a sequence of coordinate between the connected component of white pixels and that of black pixel, and by recording the locality relationship of these borders, the counters are extracted

from the binary image.

Next the fitting ellipse processing, which is also one of the functions within OpenCV, was applied. This function calculates the ellipse that fits a set of pixels (in a least-squares sense, see Fitzgibbon and Fisher, 1995). We can obtain an area and a perimeter at the same time by this processing. The circularity of the ellipse was also calculated. When this value shows 1.0 for an object, the object means full circle. The more it approaches to the value of 0.0, the more the object shows the complex and elongated polygon. We examined whether the circularity can be a useful tool to distinguish tracks from other structures (e.g., inclusions, dust, etc).

3.2.3.2. Brightness gradient in tracks and noises

As is discussed later, choice of tracks by the circularity is imperfect and other structures (e.g., inclusions, bubbles, etc.) are also detected. Therefore we apply a comparison of brightness to distinguish tracks from other noise structures. Because FT is the trail of damage formed by the two fission fragments travelling opposite directions, bottom of etched tracks (holes) shows curvature that slopes toward a point, which corresponds to the direction of fission fragment travelling. This particular shape of tracks in volcanic glass is also obvious in the profile observed

under a laser microscope (Fig. 2.5). Therefore we can see a gradual and systematic change in the brightness within that hole on the image (Fig.3.1a). By contrast, we cannot observe such a systematic change in the noises. Therefore, we examined the change in the brightness within tracks in three ways in order to distinguish the "true" tracks from the noises. The long axes of tracks and noises were acquired during the fitting ellipse processing. The pixel brightness was projected on the long axes of the ellipse, and examined to see differences between tracks and noises (see Fig. 3.2).

First, we compared a gradient (a) and a correlation coefficient (R^2) of the line fitted to all the brightness information in the structures projected against the long axis (Fig. 3.2I). Second, the brightness on the long axis is plotted and we separated the brightness profile into two areas before and after a minimum point to calculate two correlation coefficients ($R^2 1$ and $R^2 2$) (Fig. 3.2II). Finally, we compared the number of minimum points of the brightness profile along the long axis (Fig. 3.2 III). The gradient (a) and the correlation coefficient (R^2) were calculated from

$$a = \frac{n\sum_{i=1}^{n}\left(x_i y_i\right) - \sum_{i=1}^{n} x_i \cdot \sum_{i=1}^{n} y_i}{n\sum_{i=1}^{n} x_i^2 - \left(\sum_{i=1}^{n} x_i\right)^2} \quad \text{and}$$

$$R^2 = \frac{\left\{\sum_{i=1}^{n}\left(x_i - m_x\right)\left(y_i - m_y\right)\right\}^2}{\sum_{i=1}^{n}\left(x_i - m_x\right)^2 \cdot \sum_{i=1}^{n}\left(y_i - m_y\right)^2}$$

where x_i and y_i are a position of each pixel and the brightness in the structures, respectively and m_x and m_y are each average values.

3.3. Results and discussion

3.3.1. Choice of Image-capturing conditions

Fig. 3.1 shows an example of image processing applied to some tracks and noises. The resultant fitted ellipse shows almost correctly a shape of original tracks. However some noises were also detected as fitted ellipses, and they caused the increase in the number of counted tracks. To minimize these miscounting, we should carefully prepare a sample to avoid scratches or dusts on the surface and to make many screens observable.

Table 3.2 shows results of the number of counted tracks under the various capturing conditions. The number of counted tracks in x40 is anomalously larger than the number of observed tracks. Because the depth of focus is bigger with x40 than x100 objectives, many scratches, inclusions or dusts are recorded on the image (Fig. 3.3). Therefore, the image by x100 objectives is preferable even though we

need observation of more screens to count significant number of tracks.

When we compare the results between the images with different focuses, the number of counted tracks for “focus above the surface“ and “focus on the internal surface” in x100 is markedly smaller than that of the observed tracks. Because the image is dim, the Laplacian filter could not correctly detect the edge of several tracks (Fig. 3.4). Therefore, some of tracks cannot survive the binarization process. As is expected, the focus must be set on the surface strictly. Fig. 3.5 shows the effect of focus on the binarization process within the focus of ± 1.5 μm from the surface. The original images with gray scale, the images after binarization, and the images after fitting ellipse are shown for each image. We can see that no tracks are detected when the focus is on the internal surfaces. By contrast, the tracks are successfully and correctly detected when the focus is above the surfaces, provided that the focus should set on the surface within 1μm.

The numbers of observed tracks taken under the brightness 5 for x100 are slightly higher than that of the tracks taken under the brightness 4, while the brightness 5 results in underestimate in number of the tracks. When the brightness is brighter, the difference between background and the structures is clearer. Therefore it is easier to

detect the structures in the brightness 5, however, the much more noises were also detected in the brightness 5. On the other hand, the number of tracks in the brightness 4 is smaller than that of tracks in the brightness 5, however the counted noises are also small. As is shown later, undetected tracks become detected after additional etching. Therefore we suggest that the image capturing under the brightness 4 to minimize the contamination of noises.

3.3.2. Effect of etching in detection of tracks

Several tracks, whose incidental direction is very shallow, hadn't been counted under any conditions after the etching of 60 sec. These tracks are small and very shallow (see Fig. 3.1). As a result, there are only small differences in the brightness values between these tracks and background, therefore the image processing mentioned above couldn't detect these tracks. These tracks become detected when the samples are etched more heavily. Fig. 3.6 shows the example of track detection through stepwise etching. These tracks hadn't been detected after first weak etching. However, they could be counted after the additional 15 seconds etching because the track size became bigger by a stepwise etching.

3.3.3. Distinction of the tracks from the noises

The numbers of detected tracks as ellipses for the focus on the surface are still higher than that of observed tracks. Therefore, we examined the methods to separate the "true" tracks among ellipses. We firstly tried the circularity for a distinction of the tracks from the noises, because tracks show the limited circularity. When the circularity of tracks are measured by ImageJ (Schneider et al., 2012), they mainly fall in 0.65 - 1.0 (Fig. 3.7).

The numbers of detected tracks are increased when wide range of the circularity is applied because the structures other than FTs are also counted (Table 3.2). When we measure the circularity of the tracks, we firstly must convert original images into binary images on the ImageJ. Most of images were easily converted into the binary images and tracks show correct shapes. However one track whose incidental direction was quite shallow didn't show correct shape and the track show elongated polygon. The circularity of this erroneous image of track was lower (0.52) than that of the normal tracks. Most of structures between 0.00 - 0.65 must be noises, therefore we apply circularity (0.65 - 1.00) in order to detect the number of "true" tracks more correctly, though several noises are also detected in this circularity range.

Next we show results of the change in the brightness within tracks and noises examined in three ways (Fig. 3.2). We examined images taken in the brightness 4 and brightness 5 for comparison. Fig. 3.8 shows some examples of the pixel brightness within tracks and noises along the long axis of ellipse. Generally the profiles of tracks have only one peak, however the profiles of noises have no peak or multi-peaks. Fig. 3.9 is the result of the gradient (a) and a correlation coefficient (R^2) of the brightness in the structures (see Fig. 3.2I). Most of tracks and noises show high R^2 values, however some tracks show low R^2 values. No difference is found between the gradients of tracks and noises. Fig. 3.10 shows the result of two correlation coefficients ($R^2 1$ and $R^2 2$) of the brightness calculated from the fitted lines along the long axis (see Fig. 3.2II). Both of correlation coefficients show no difference between the track and the noises and also have no difference between the brightness 4 and brightness 5. The number of minimum points on the long axes in the structures is shown in Table 3.3 (see Fig. 3.2III). Most of tracks have only one minimum point in both brightness, while the noises have zero or more than two points (see also Fig. 3.8). However several noises were also detected as having one minimum point in the brightness 5, because the too much light eliminates the

delicate topographic difference in a structure (Fig. 3.8b). On the other hand, no noises have one minimum points in the brightness 4 partly due to the small number of total of counted noises. Therefore we should choose the brightness 4 in order not to detect unnecessary noises, and we can find the ”true” tracks among the structures using the counting of minimum points in the brightness on the long axis.

3.4. Discussion and Conclusion

This study proposes a new FT counting strategy for volcanic glass using image processing. Images must be acquired using x100 objective lens under brightness 4 (2.3 – 2.4 klux), and the focus must be on the surface within 1 micron above. This preferable setting will be a subject of microscope and camera combination. Ellipse fitting detects both of tracks and other structures such as inclusions, dusts, etc. To distinguish ”true” tracks from other structures, circularity and the number of minimum points in the brightness profile along the long axis of ellipse are effective. Some of the tracks were not detected at an earlier etching condition, however, they become detected after additional etching. As was proposed by Ito and Hasebe (2011), observation of increase in number of tracks through the stepwise etching to estimate the number of tracks per a unit volume is one of the procedures to eliminate the

effect of track reduction at ambient conditions (e.g. Wagner, 1979; Naeser et al., 1980 etc.). When we apply this procedure to measure a FT age, the image processing can detect the all tracks including small and very shallow tracks. However there is a possibility to count some types of noises as tracks. These miscounted noises may result in overestimation of ages. The effect of miscounting varies depending on the track density, and for this sample with the track density of 3030 (/cm^2, Kitada et al, 1994a), we can estimate the effect of noises may be less than 5% (1 noise out of 30 tracks). For sample with higher track density, the effect must be smaller.

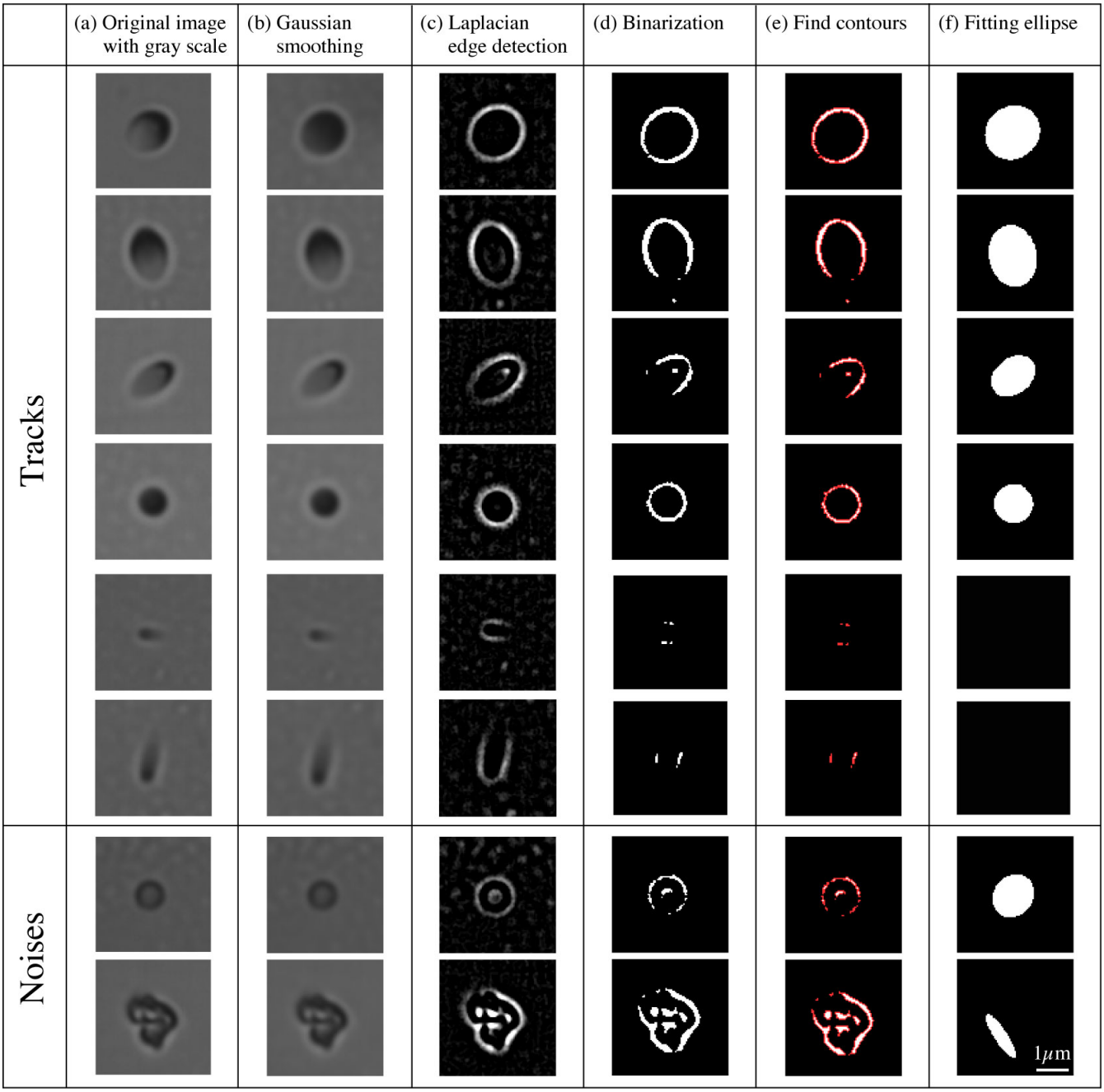

Fig. 3.1
Images of tracks and noises after each image processing. Actual coordinates of the contours are shown as red lines on the images after Find contours procedure (e).

Table 3.1
Image capturing conditions.

Magnification of objective lens	x40	x100
Brightness	(1) 0.15 - 0.17 klux (2) 0.48 - 0.50 klux	(3) 1.20 - 1.30 klux (4) 2.30 - 2.40 klux (5) 4.10 klux (Max)
Focus	On the surface, above the surface or on the internal surface	
Light source	Transmitted light	

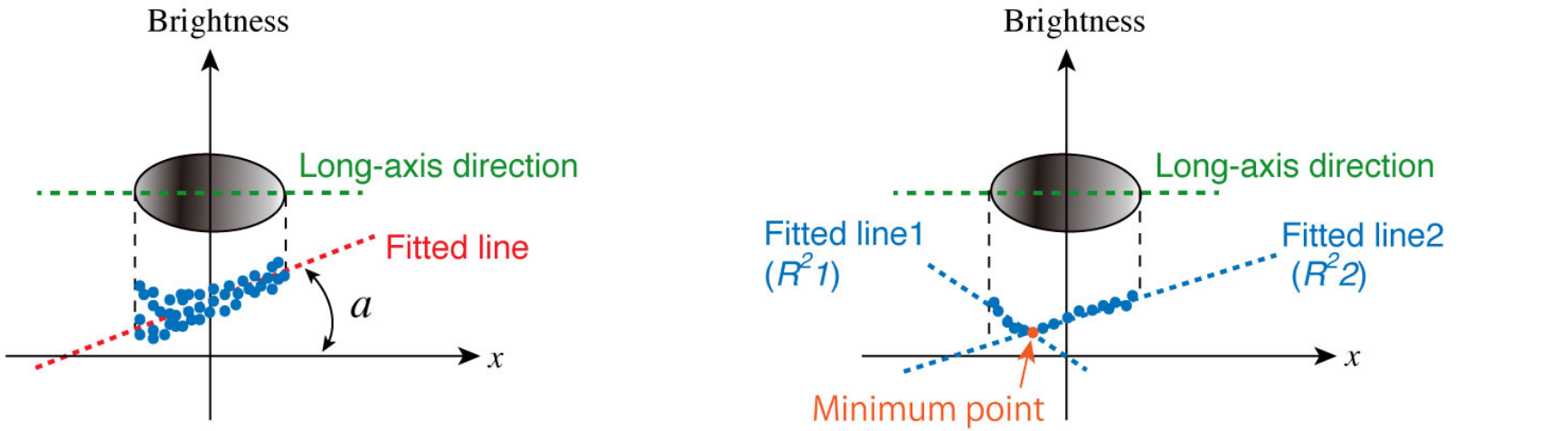

(I) Gradient (a) and a correlation coefficient (R^2) for the line fitted to all the brightness information in the structures

(II) Calculaton of two correlation coefficients (R^2*1* and R^2*2*)
(III) Comparison between the number of minimum points in the structures

Fig. 3.2
Three types of acquisition of the brightness in the structures.

Table 3.2

Result of the number of counted tracks under the various capturing conditions. Left value and right value in parenthesises for focus on the surface show the number of counted "true" tracks and that of counted noises, respectively. Number of observed screens is 69 and 30 for x40 and x100, respectively.

(a) Focus above the surface

Objective lens	x40		x100		
	Brightness 1	Brightness 2	Brightness 3	Brightness 4	Brightness 5
Circularity (0.00 - 1.00)	112	177	1	6	8
Circularity (0.50 - 1.00)	76	106	1	3	5
Circularity (0.65 - 1.00)	55	69	0	1	3
Circularity (0.75 - 1.00)	33	43	0	0	1
Circularity (0.85 - 1.00)	9	21	0	0	0
Observed track counts	25		34		

(b) Focus on the surface

Objective lens	x40		x100		
	Brightness 1	Brightness 2	Brightness 3	Brightness 4	Brightness 5
Circularity (0.00 - 1.00)	376	374	9	41 (26 + 15)	53 (29 + 24)
Circularity (0.50 - 1.00)	200	225	8	32 (26 + 8)	48 (29 + 19)
Circularity (0.65 - 1.00)	115	149	8	30 (26 + 4)	41 (29 + 12)
Circularity (0.75 - 1.00)	64	98	4	29 (26 + 3)	36 (29 + 7)
Circularity (0.85 - 1.00)	22	41	2	22 (22 + 0)	28 (27 + 1)
Observed track counts	25		34		

(c) Focus on the internal surface

Objective lens	x40		x100		
	Brightness 1	Brightness 2	Brightness 3	Brightness 4	Brightness 5
Circularity (0.00 - 1.00)	362	363	0	3	3
Circularity (0.50 - 1.00)	256	248	0	2	2
Circularity (0.65 - 1.00)	203	170	0	2	2
Circularity (0.75 - 1.00)	142	117	0	1	1
Circularity (0.85 - 1.00)	62	38	0	0	0
Observed track counts	25		34		

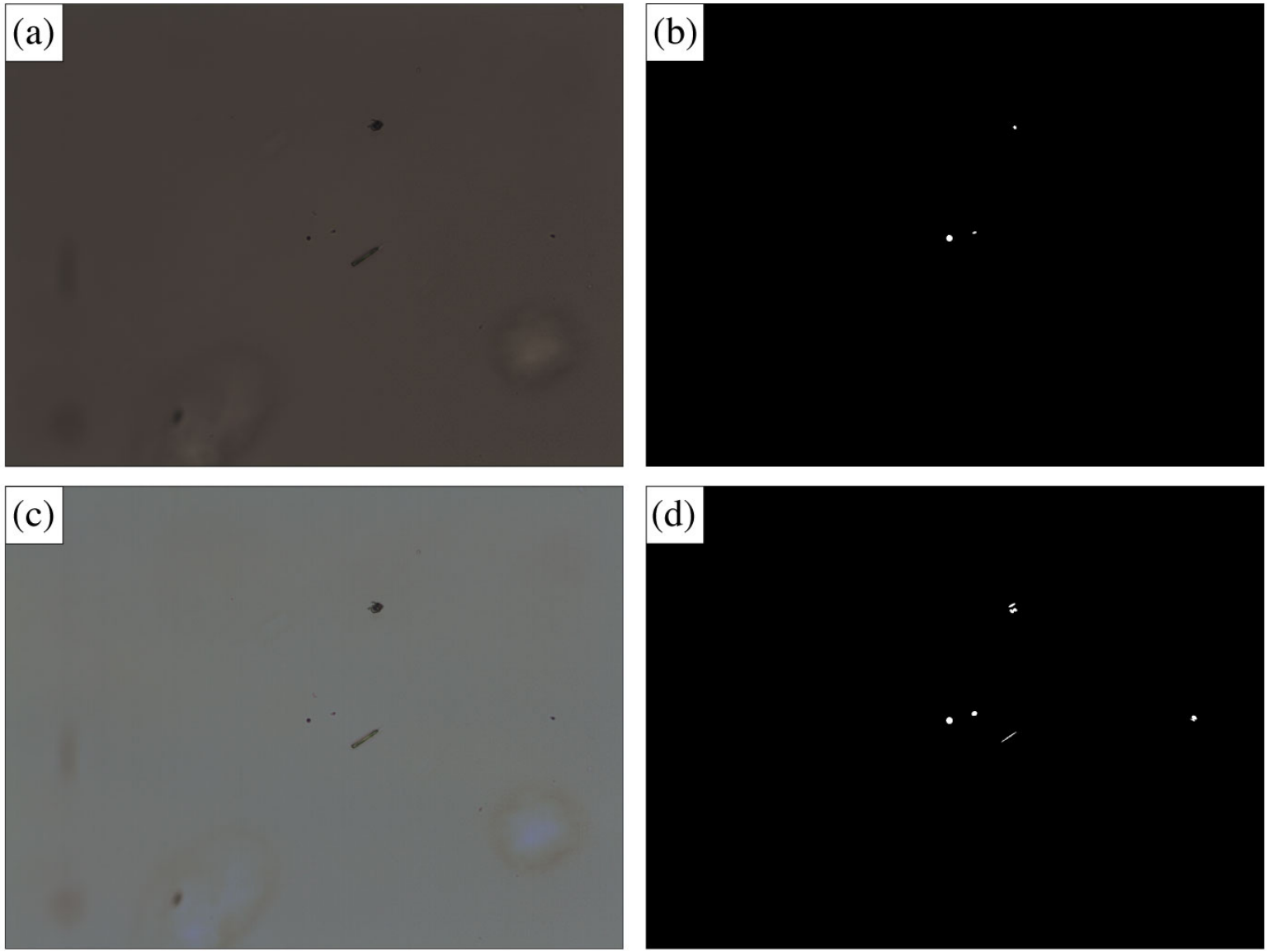

Fig. 3.3

Examples of images with x40 objective. (a) Original image in the brightness 1. (b) Image after fitting ellipse procedure of image (a). (c) Original image in the brightness 2. (d) Image after fitting ellipse procedure images of image (c).

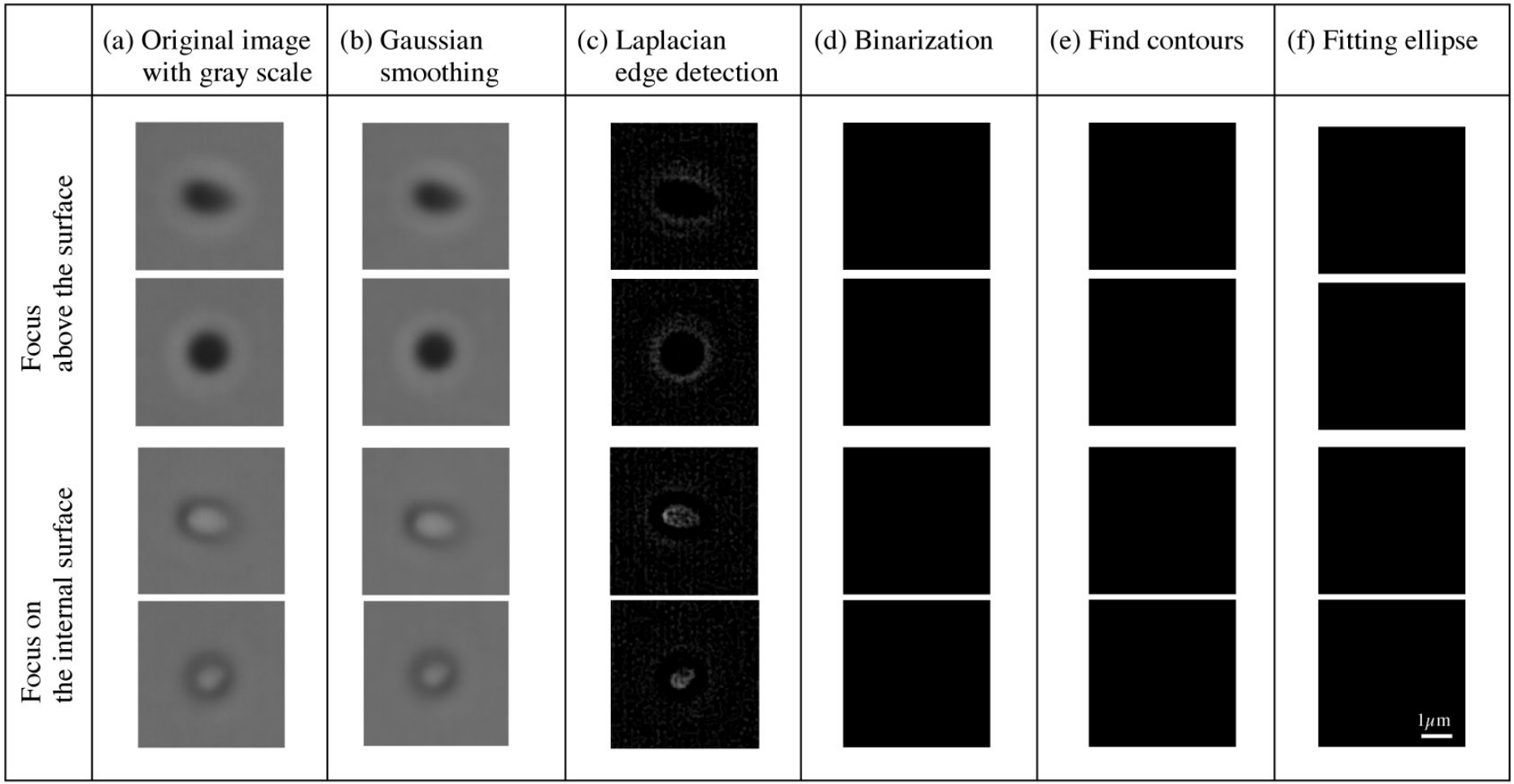

Fig. 3.4
Examples of image processing for the tracks in defocused images.

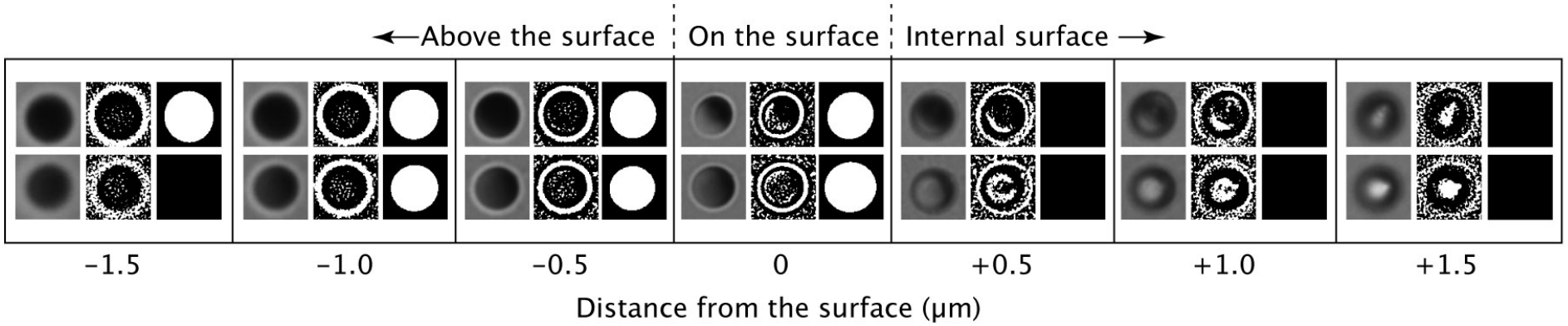

Fig. 3.5
Effect of the focus in image processing is shown on representative two tracks which are captured with the different focuses within ± 1.5 μm from the surface. Each image shows the original images with gray scale, the images after binarization and the images after fitting ellipse.

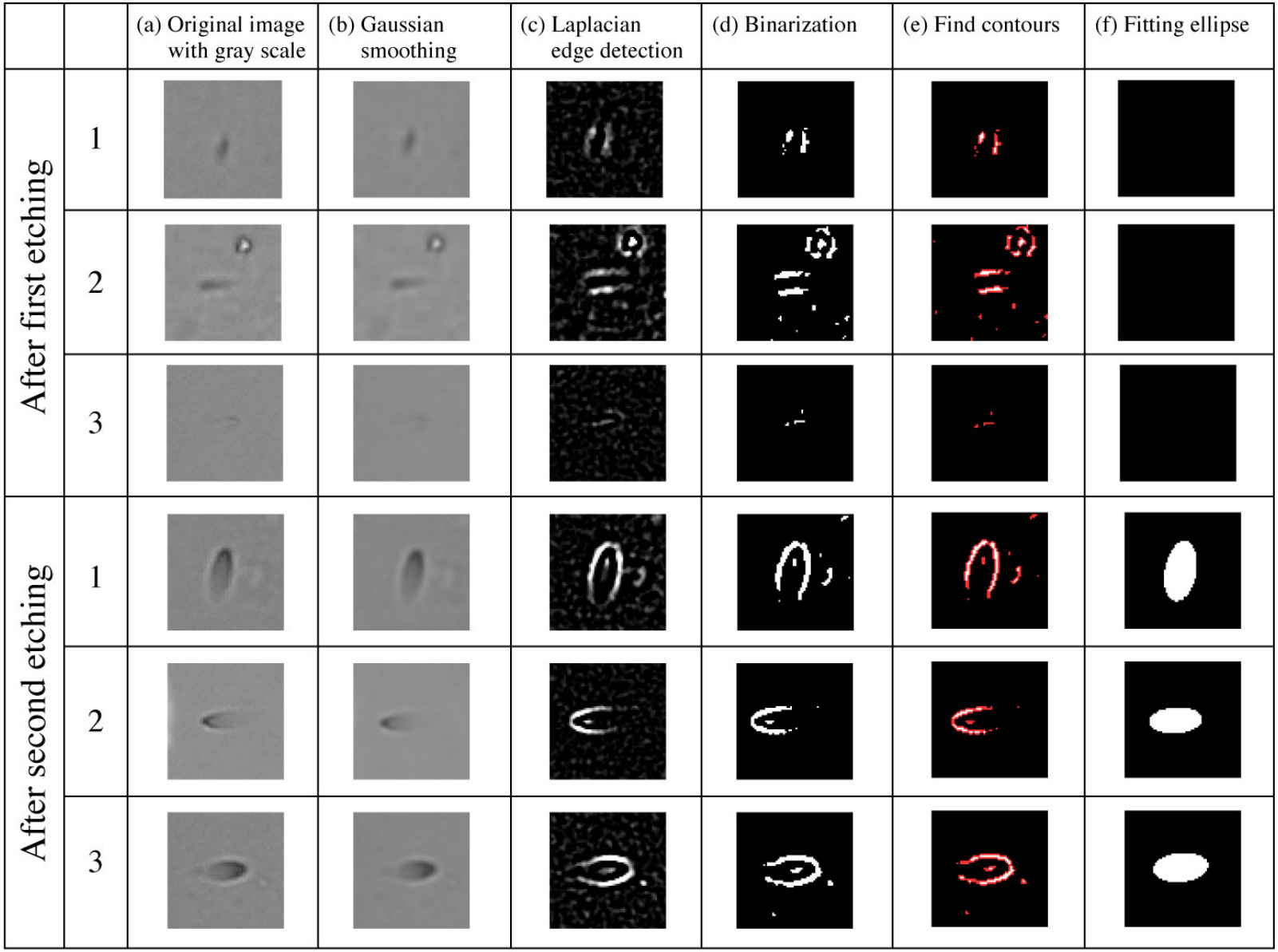

Fig. 3.6

Effect of etching conditions on small tracks (tracks with shallow incident angles). Etching condition is written below the figure.

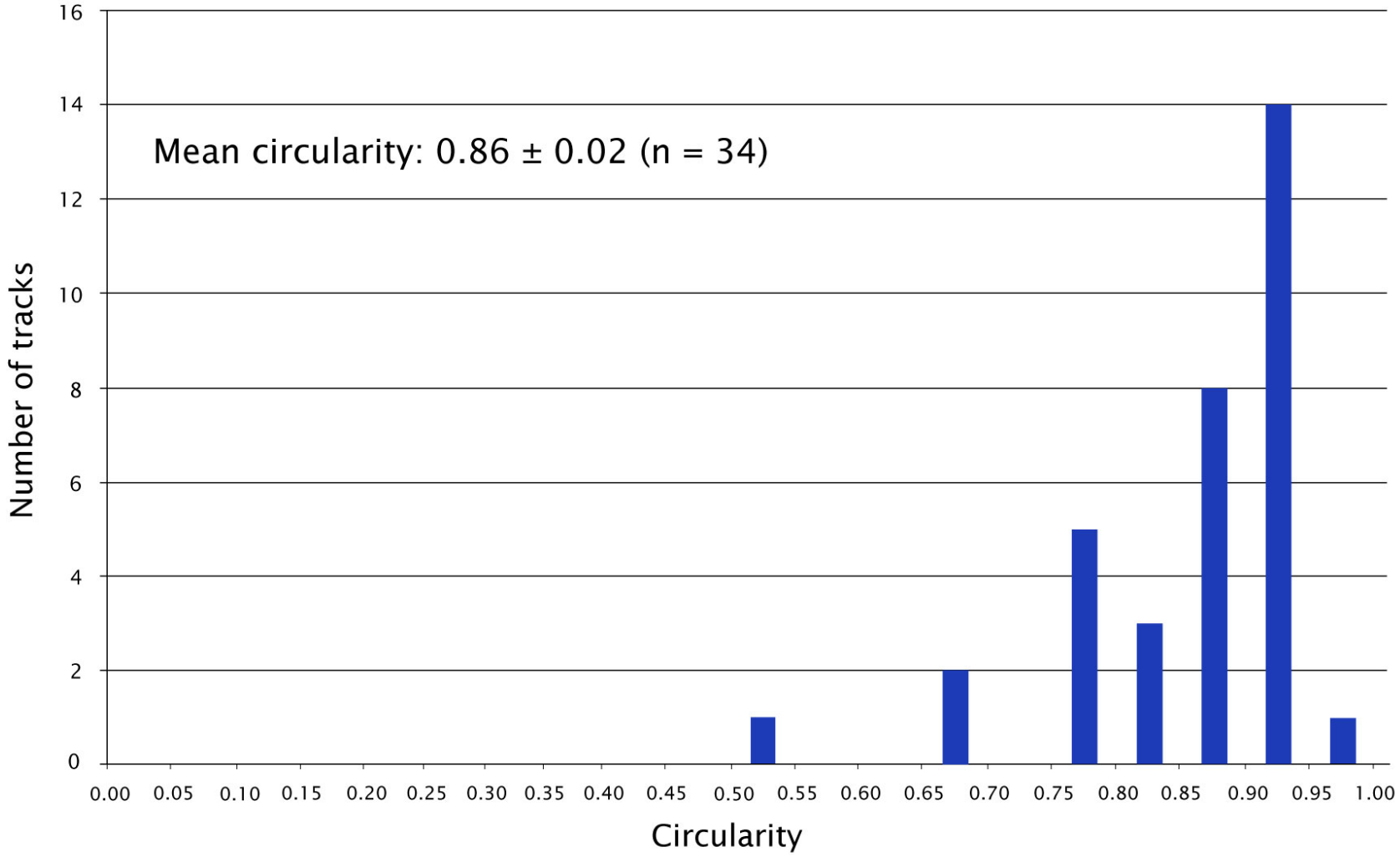

Fig. 3.7
Result of circularity measurement for ”true” tracks. The circularity was measured using ImageJ. The circularity of tracks mainly fall in 0.65 - 1.00.

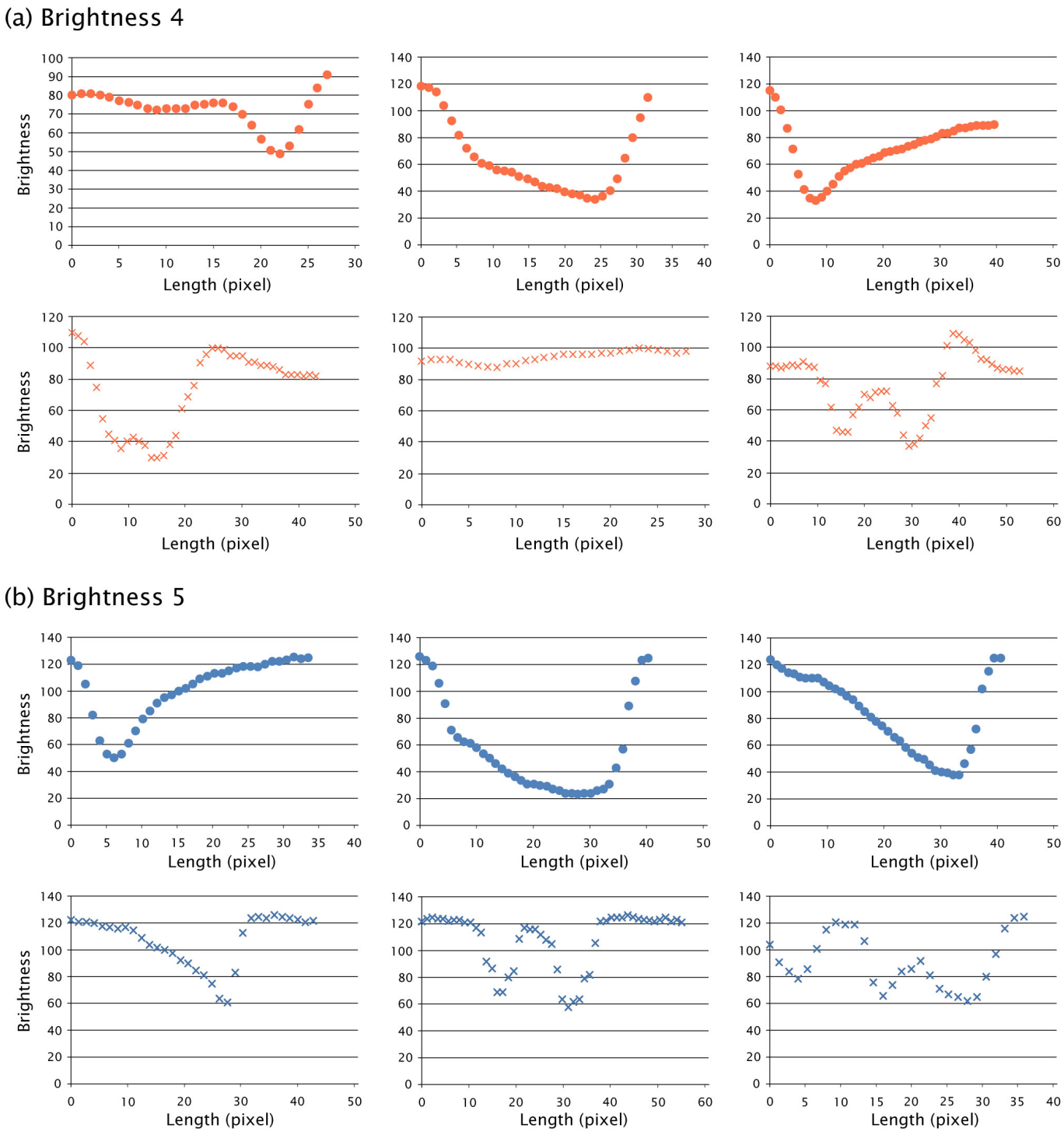

Fig. 3.8
Examples of the profiles on the long axis in the brightness 4 and 5. Circles and crosses represent tracks and noises, respectively.

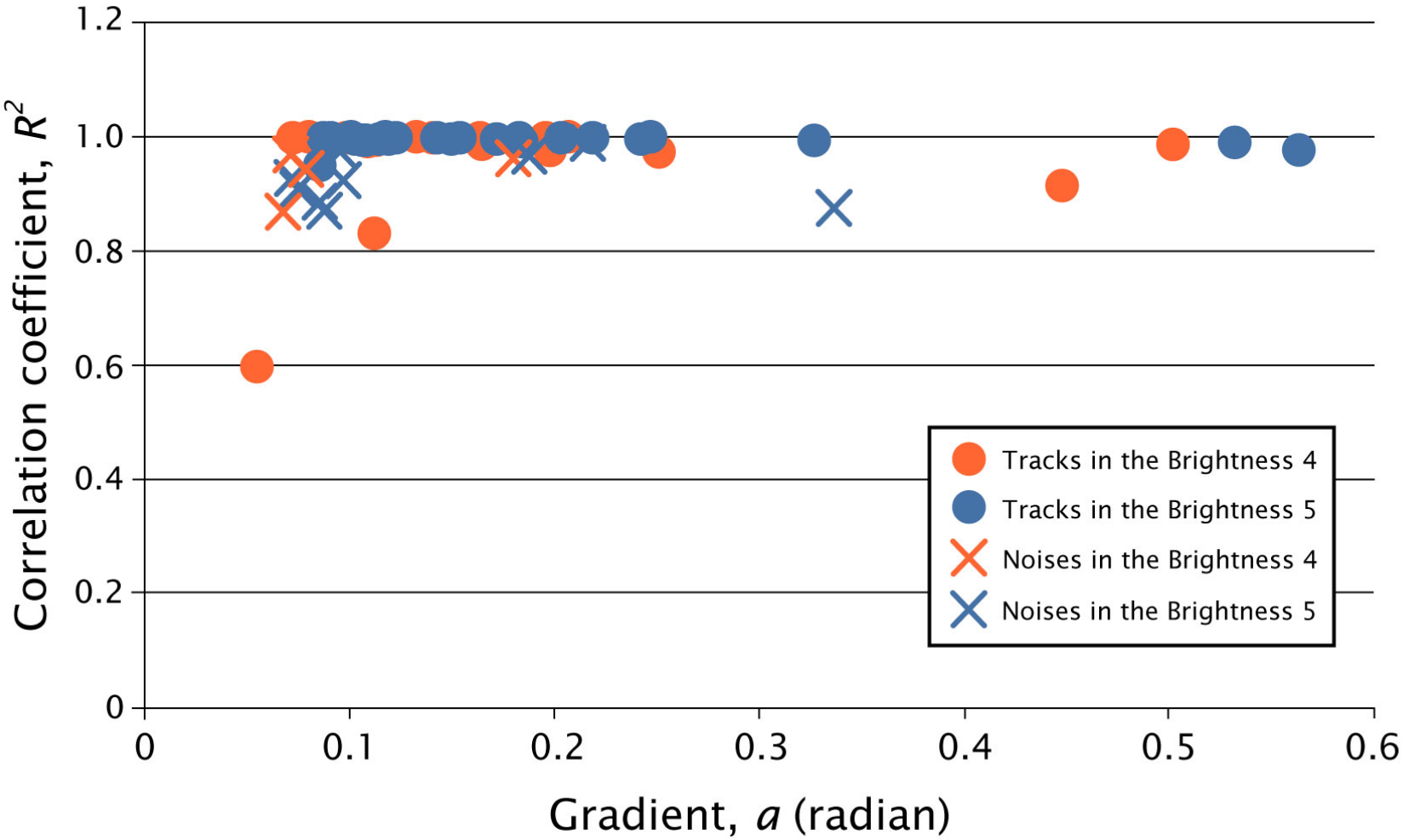

Fig. 3.9
Result of the gradient (a) and the correlation coefficient (R^2) of the brightness in the structures (see Fig. 3.2 I). Circles and crosses represent tracks and noises, respectively.

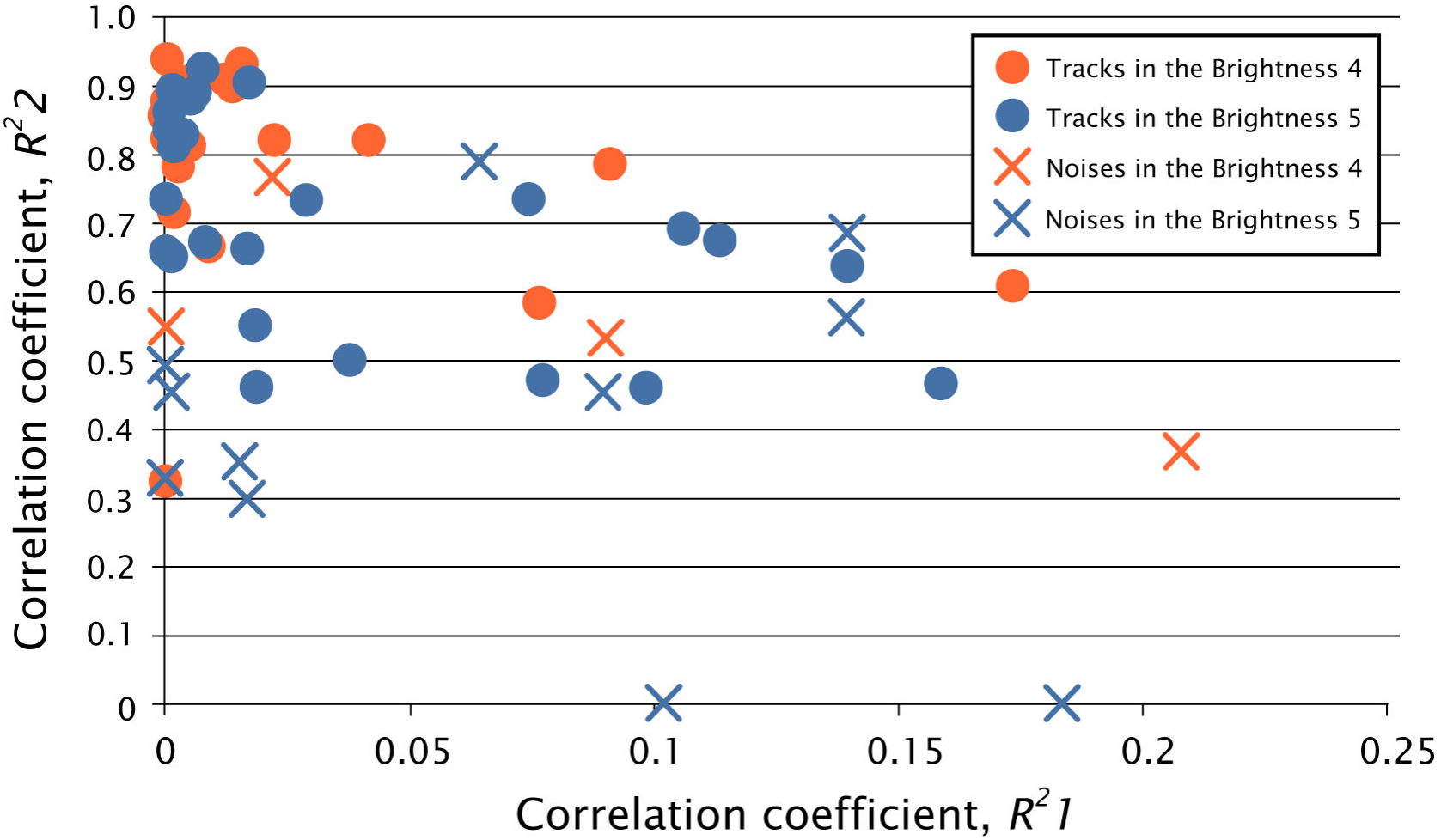

Fig. 3.10
Result of two correlation coefficients ($R^2 1$ and $R^2 2$) of the brightness calculated from the fitted lines along the long axis (see Fig. 3.2II). The brightness profile was separated into two areas before and after a minimum point. Circles and crosses are tracks and noises, respectively.

Table 3.3
Result of the number of minimum points on the long axes in the structures.

Minimum points	Brightness 4		Brightness 5	
	Tracks	Noises	Tracks	Noises
0	1	1	0	2
1	24	0	27	5
2	1	2	2	4
3	0	1	0	1

Chapter 4:

Alpha - Recoil Track counting using atomic force microscope in zircon

4.1. Introduction

Widespread tephras are important time markers for correlating the geology of different regions. Eruption ages of the tephras have been analyzed by various geochronological methods. K-Ar method can be applied to several minerals (e.g. feldspars, mica, amphibole or volcanic glass) which are included in tephras. However, K-rich minerals in tephra sometimes lose radiogenic Ar during secondary hydration and devitrification especially for glass, and hence underestimated ages were reported (Kaneoka, 1972; McDougall and Harrison, 1988). Radiocarbon (^{14}C) method is applicable to inorganic or organic deposits (e.g. Aitken, 1990; Black, 1975; Hildreth, 1981; Miller and Smith, 1987), though materials containing carbon are rarely associated with active lava flows and the technique's dating range is limited to up to around 40,000 years (Fattahi and Stokes, 2003). Luminescence method is also able to apply to several minerals (e.g. feldspar, glass and quartz) in most volcanic products, though problems of the method include such as a type of

signal instability called *anomalous fading* of blue luminescence from feldspar in basaltic deposits (Wintle, 1973; Wintle, 1974); the poor signal-to- noise ratio of many quartz and glass thermoluminescence and optically stimulated luminescence analyses (Berger and Huntley, 1994; Miallier et al., 1991). Thus, each method has its advantages and disadvantages, therefore, an improvement of the conventional age dating methods is needed, together with the development of new dating methods.

Recently new observation techniques are reported for the fission track dating. Ohishi and Hasebe (2012) proposed use of atomic force microscope (AFM) to count tracks in zircon with high track densities. Scanning electron microscopy (SEM) is also used sometimes for a detailed investigation of track size and shape (e.g. Monnin, 1980; Seitz et al., 1973). These observation methods indicate a possibility of FT dating with high track densities after relatively short etching periods, and may be able to date samples that could never have been dated. Especially, the observation with a resolution of the nano-scale (Brown and Liu, 1996; Johnson et al., 2009; Yasuda et al., 2001; Zagorski et al., 2003) enables the observation of smaller structures than FTs. Ohishi and Hasebe (2012) reported FT counting using AFM, however, they also observed many shallow pits on the same images. These pits don't

disappear and develop after chemical etching, therefore they may be alpha-recoil tracks (ARTs). The ARTs are produced by the decay of uranium (thorium) such that an alpha particle is emitted and the daughter nucleus recoils in the opposite direction (Huang and Walker, 1967) giving rise to recoil damage. Generally, the etch pits are so shallow that they are essentially invisible in ordinary bright-field optical microscopy because the range of the recoil length is only a few tens of nanometres (Brown and Liu, 1996). Natural ARTs are successfully observed in only mica (e.g. Brown and Liu, 1996; Dartyge et al., 1981; Hashemi-Nezhad, 1998; Huang and Walker, 1967). The number of the ARTs is much larger than that of FTs because the decay constant for α-decay is large (= 8.5×10^{-17} a^{-1}, 1.5×10^{-10} a^{-1} for spontaneous fission). Therefore it has a possibility to apply Quaternary events.

In this study, we tested for observation of alpha recoil tracks (ART) in zircon using AFM. Unlike the electron microscope, AFM is able to observe a mineral surface without special pre-treatment, such as carbon coating. High resolution can be obtained readily under atmospheric conditions. Firstly we observed the surface of young zircons under the AFM to see the structures found in old zircons exist or not. The young zircons have no ARTs because they were produced in recent years,

therefore if the shallow pits are ARTs, they should not be observed in young zircon. Secondary we examined the effect of annealing for old zircons. If shallow pits are ARTs, they must be disappeared when crystals heated and damages healed. A size reduction of ARTs is also observed through the annealing experiment.

4.2. Samples and preparations

We observed three types of zircons (YS18-1, UHLv1 and OD-3). The YS18-1 was from Indonesia and that size was about 100μm × 60μm. The reported FT age is 0.32 ± 0.05 Ma (Table 4.2). The UHLv1 was from Unzen volcano that erupted in 1991 to 1996 in Nagasaki Prefecture, Japan. The size of zircons was about 100μm × 70μm. These two zircons were used to examine whether there are the structures like ARTs or not.

The OD-3 was collected from the Mihara body of the Kawamoto Granodiorite in Simane Prefecture, southwest Japan and the grain size is up to 0.75 mm. The sample does not show a marked zoning and has few inclusions. The concentration of uranium is from 100 to 1200 ppm and has a homogeneous distribution in a grain (Iwano et al., 2012; Iwano et al., 2013). The reported FT age and U-Pb age is 33.0 ± 1.0 (2σ) Ma and 33.04 ± 0.10 Ma (2σ), respectively (Iwano et al, 2012; Iwano et al,

2013). Generally, an alpha track density observed per unit area is the fuction of sample age, ^{238}U, ^{235}U and ^{232}Th concentrations, and a track size of ARTs. Ohishi (2012MS) estimated the alpha track density of OD-3 given total U and Th concentrations (U = 300 ppm, Th = 100 ppm), U isotopic ratio (^{238}U : ^{235}U = 0.993 : 0.007), FT density (6.5×10^6 counts / cm^2), ARTs diameter (15×10^{-7} cm) and FT length (5.25×10^{-4} cm). Then, the estimated alpha track density is 4.0×10^4 ($\times 10^6$ counts / cm^2) (Table 4.2). This sample was used for the annealing experiment under 600°C or 1000°C for 1-hour.

We prepared the samples according to Ohishi and Hasebe (2012). Firstly, the zircons were mounted in PFA Teflon and then ground on wet abrasive paper (#1500) to expose internal surface. Then, the sample was polished with diamond paste of 15-μm, 3-μm, 1-μm sizes, 0.5-μm sizes and 0.125-μm sizes. In this study, we examined further polish using colloidal silica (from 0.02 to 0.06-μm sizes).

Samples were etched with eutectic melt mixed with an equal mole of NaOH and KOH at 230 °C (Gleadow et al., 1976). The etching time is 10 hours for the YS18-1 and the UHLv1, 2 hours for the OD-3.

We used the Nanofinder®HE (TOKYO INSTRUMENTS, INC.) for the YS-18-1

and the UHLv1 and the NanoWizard®II (JPK Instruments) for the OD-3. Details of the analysis are presented in Table 4.3. Each AFM was used in the AC mode (non-contact mode) for surface topography analysis. The AFM probe for the AC mode consisted of a silicon conical tip of height 14 μm, of cone angle 0 °, and radius of curvature 7 nm. The optimized scan parameters for this prove is resonance frequency of 200 - 400 kHz, and the spring constant of 8.4 -57 N/ m^{-1}. The samples were scanned and characterized in air at room temperature, and the corresponding topographic surface images were recorded. All profiles were scanned for perpendicular to the crystallographic c-axis.

4.3. Results and Discussions

The AFM image showed the highest point in the light color and the lowest point in the dark color. Green line on the AFM images show the position of cross-section and each profile is shown below the AFM images. Horizontal axis is the position (μm) and vertical axis is the height (nm).

4.3.1. Results and discussion of the observation of young zircons

Fig. 4.1 and Fig. 4.2 show topographical images and cross-sections for YS18-1 and UHLv1. Cross sections showed cyclic wave profile, and the wavelengths of

which were about 0.5 – 1.0 μm for YS18-1 and less than 0.5 μm for UHLv1. These wavelengths are slightly longer than the traces of polishing scratches (final polishing was done using 0.02 – 0.06 μm colloidal silica) while the final polishing was parallel to the c-axis. Thus these profiles with both samples correctly reflect original structures. Moreover amplitudes of the profiles with both samples are about 1 – 2 nm, and the surfaces of both samples show quite flat in comparison with the amplitudes (> 4 nm) of the profiles by Ohishi and Hasebe (2012). Therefore both samples might have been little affected by radiation damages (especially ART). On the other hand, some small pits were observed in UHLv1 (Fig. 4.2). The small pits (a depth is 4 - 6 nm and a width is about 0.5 μm) look like FT when compared with the AFM images reported by Ohishi and Hasebe (2012), however the pits are quite small in comparison with FT geometry. Additionally the decay constant for spontaneous fission (8.5×10^{-17} a^{-1}) is much smaller than that for α-decay (1.5×10^{-10} a^{-1}), and it must be extremely difficult to find FTs in these modern volcanic samples. Therefore the observation result indicates that the pits would be ARTs. The pit depth is compatible with the amplitude of surface structure found in old samples (> 4nm, Ohishi and Hasebe, 2012).

4.3.2. Results and discussion of annealing experiment

Fig. 4.3 and Fig. 4.4 show topographical images and cross-sections after 600°C and 1000°C annealing, respectively. These images are enlarged 3 μm × 3 μm squares. We can also see cyclic wave profile on the sample surface, and the samples under both temperatures showed smooth surfaces. The amplitudes in the profile were about 15 - 30 nm and about 5 – 15 nm for 1-hour annealing at 600°C and 1000°C, respectively. A wavelength of the sample is about 0.2 μm and less than 0.1 μm at 600°C annealing and 1000°C annealing, respectively. We can also find a pit like FT on the sample at 600°C annealing (Fig. 4.3). The depth of the pit is about 30 nm, and a shape of the pit show cone shape. On the other hand, FTs couldn't been found on the sample at 1000°C annealing (Fig. 4.4) because FT had disappeared by exposing to high temperatures. Thus the pit, which we observed on the sample at 600°C annealing, seems to be FT because of short annealing time (1-hour). Surface waveform reported in Ohishi and Hasebe (2012) show the amplitude of less than 10 nm. Compared with their topographical images, no difference is found between non-annealed sample and annealed sample at 600°C and 1000°C. Therefore it seems that the ARTs can be annealed more than 1000°C.

4.4. Conclusion

In this study, cyclic surface structures were successfully recognized in the AFM images, the structures in young sample (YS18-1 and UHLv1) were quite flat, and the original structures in the samples were successfully observed. In addition, we observed the pits, which are very small and shallow in UHLv1. The pits might be ARTs.

Cyclic surface structures are also observed in old zircon (OD-3) after high annealing temperatures. FT is still observable on the zircon after 600°C annealing for 1-hour, further the cyclic wave also observed after 1000°C annealing. Therefore the ARTs might be able to be annealed more than 1000°C. To apply ART dating, further understanding on how ART looks like on AFM or other nano-scale imaging must be necessary.

Chapter 5: General conclusions

This doctoral thesis proposes a new FT dating methodology for volcanic glass and a potentiality for development of new dating method using ARTs in order to know further information of Quaternary volcanic history. Chapter 2 shows new FT dating that estimates the uranium concentration in LA-ICP-MS analyses and the track number per unit volume from observations of the number of tracks and track geometry in stepwise etching. With a view to make this method more practical, an automated track recognition system would be a powerful tool to increase the number of tracks counting in stepwise etching. Therefore, new FT counting strategy for volcanic glass is also proposed using image processing in chapter 3. Images must be acquired using x100 objective lens under brightness 4 (2.3 – 2.4 klux), and the focus must be on the surface within 1 micron above. To distinguish ”true” tracks from other structures, circularity and the number of minimum points in the brightness profile along the long axis of fitted ellipse are effective. Some of the tracks were not detected at an earlier etching condition, however, they become detected after additional etching. When this procedure is applied to measure a FT age, the image processing can detect the all tracks including small and very shallow tracks. Finally,

in chapter 4, the development of new age dating using ARTs is also examined in order to cross-check the ages which were provided using another age dating in same tephra. Cyclic surface structures were successfully recognized in the AFM images. The structures in young sample (YS18-1 and UHLv1) were quite flat, and the original structures in the samples were successfully observed. In addition, the pits, which seem to be ARTs were also observed in UHLv1. Cyclic surface structures are also observed in old zircon (OD-3) after the annealing at high temperatures. FT is still observable on the zircon after 600°C annealing for 1-hour, and the cyclic wave still observed after 1000°C annealing. Therefore the ARTs might be able to be annealed at more than 1000°C. To apply ART dating, further understanding on how ART looks like on AFM or other nano-scale imaging must be necessary.

These improvements and development may provide more important ages for Quaternary chronology and the ages may be a helpful lead to reconstructing Quaternary volcanic history.

Table 4.1
A selection of Quaternary dating methods applicable to volcanic deposits (from Aitken, 1998 with modification in Fattahi and Stokes, 2003).

Method	Age range (ka)	Material dated	Applicability for volcanics	Limitations	Example
Radiocarbon	0.1–40	Wood, plant, seeds	Indirect	Need carbon, Upper age limit	Lowe et al. (1998)
Potassium–Argon, Argon–Argon	10 → 1000	potassium-rich minerals (e.g., sanidine)	Direct	Need K and Ar, Lower age limit	Bragin et al. (1999)
Fission tracks	50 → 1000	Zircon, obsidian, volcanic glass	Direct	Track fading	Bigazzi et al. (2000)
Uranium series	0.1 to ~ 800	Stalag-calcite, tooth animal	Direct	Contamination	Neymark and Paces (2000)
Luminescence	0.01 → 1000	Pottery, sediment	Direct and indirect	Error limits (~ 5%)	Miallier et al. (1994)
ESR	1 to ~ 800	Tooth enamel	Direct	Error limits (>5%)	Imai et al. (1992)
Magnetism	0.1 to 8, 100 → 1000	Stalag-calcite, pottery	Indirect	independent age control is needed	Laj et al. (2000)

Table 4.2
Referenced ages for YS18-1, UHLv1 and OD-3.

Sample	Referenced age	Alpha track density ($\times 10^6$ counts / cm^2)	Reference
YS18-1	0.32 ± 0.05 Ma	-	Unpublished
UHLv1	≒ 0	-	
OD-3	33.0 ± 1.0 Ma (2σ) 33.04 ± 0.10 Ma (2σ)	4.0×10^4	Iwano et al. (2012) Iwano et al. (2013) Ohishi (2012MS)

Table 4.3
Detail of AFM analytical setting.

	YS18-1 and UHLv1	OD-3
AFM model	Nanofinder®HE (TOKYO INSTRUMENTS, INC.)	NanoWizard®II (JPK Instruments)
Cantilever	OMCL-AC160TN-R3 (Olympus Corporation)	OMCL-AC160TN-R3 (Olympus Corporation)
Scan rate (Hz)	0.8	1.7
Scan area (μm^2)	10 × 10	24 × 24

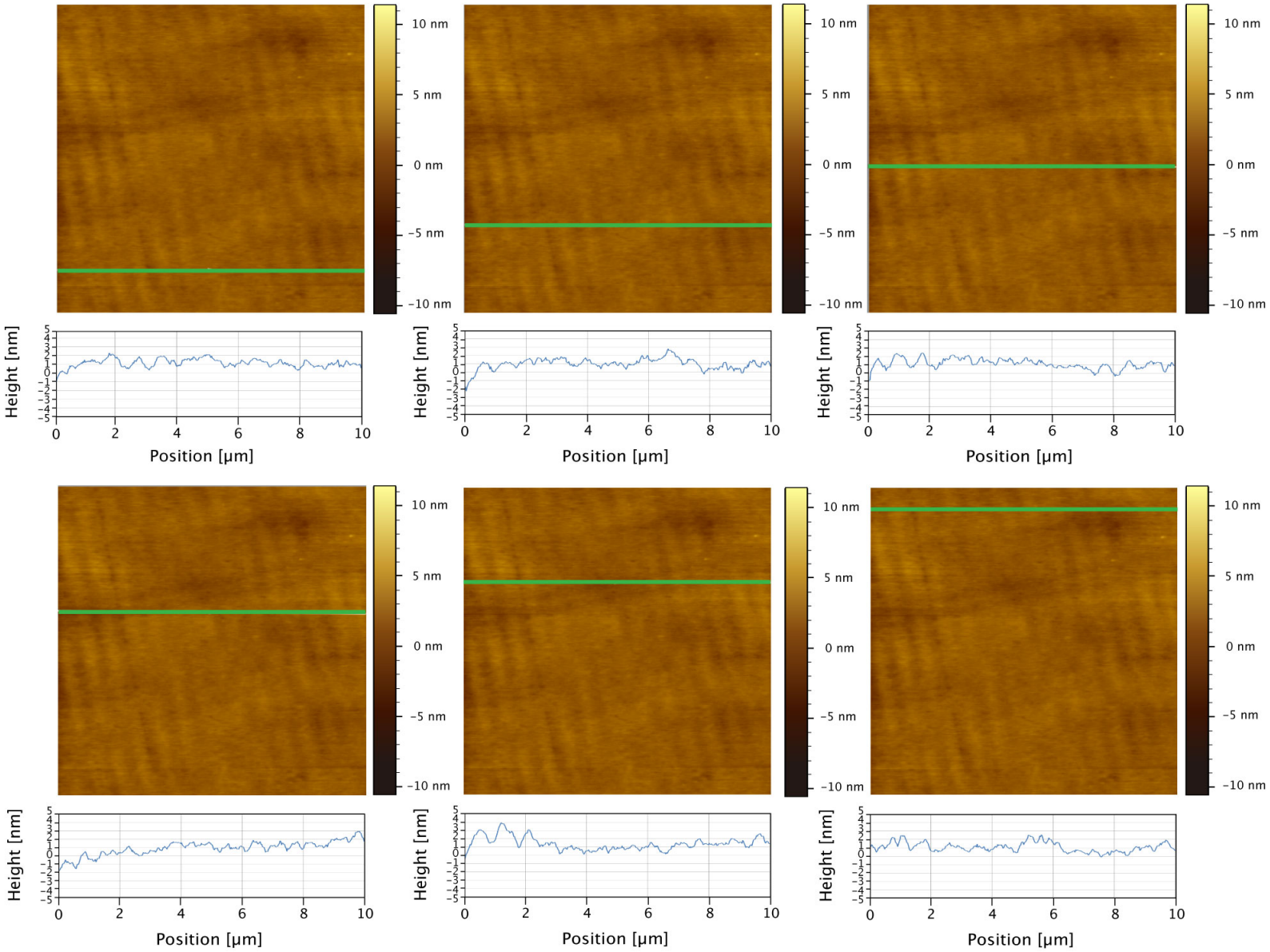

Fig 4.1

AFM images in YS18-1. Green line shows the position of each cross-section, and the profiles are below each topographical image.

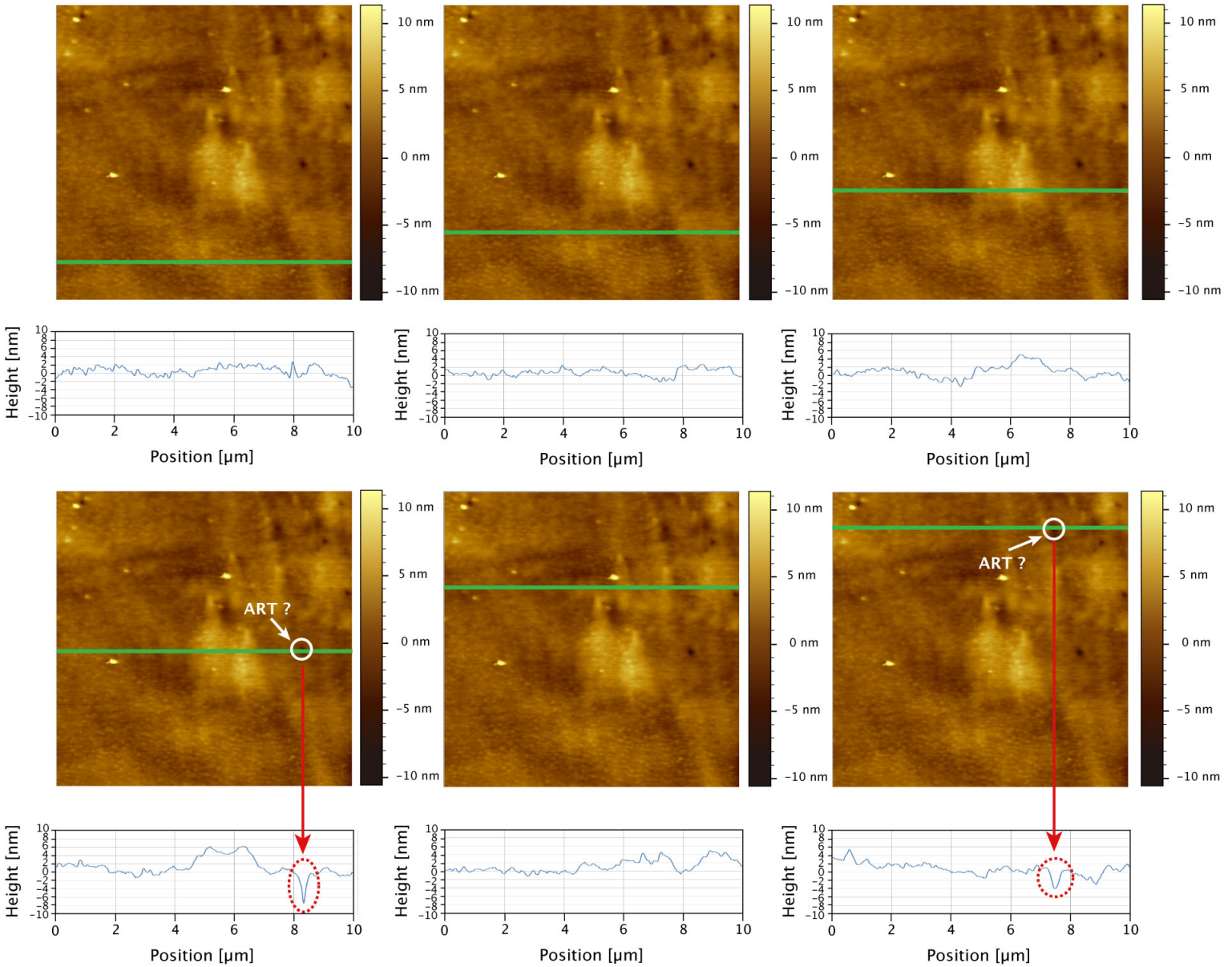

Fig 4.2

AFM images in UHLv1. Green line shows the position of each cross-section, and the profiles are below each topographical image.

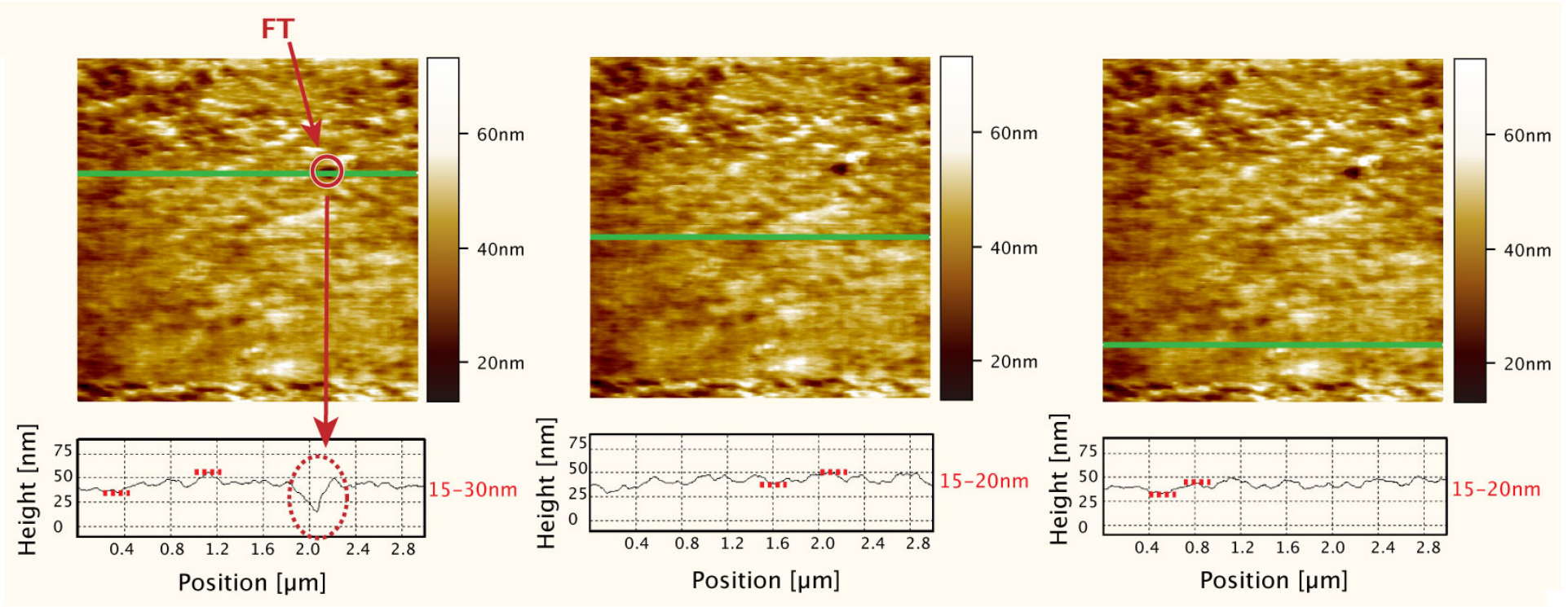

Fig 4.3

AFM images in OD-3 with 600°C annealing for 1-hour. These images are enlarged 3 μm × 3 μm squares. Green line shows the position of each cross-section, and the profiles are below each topographical image. Values beside each profile are the amplitudes.

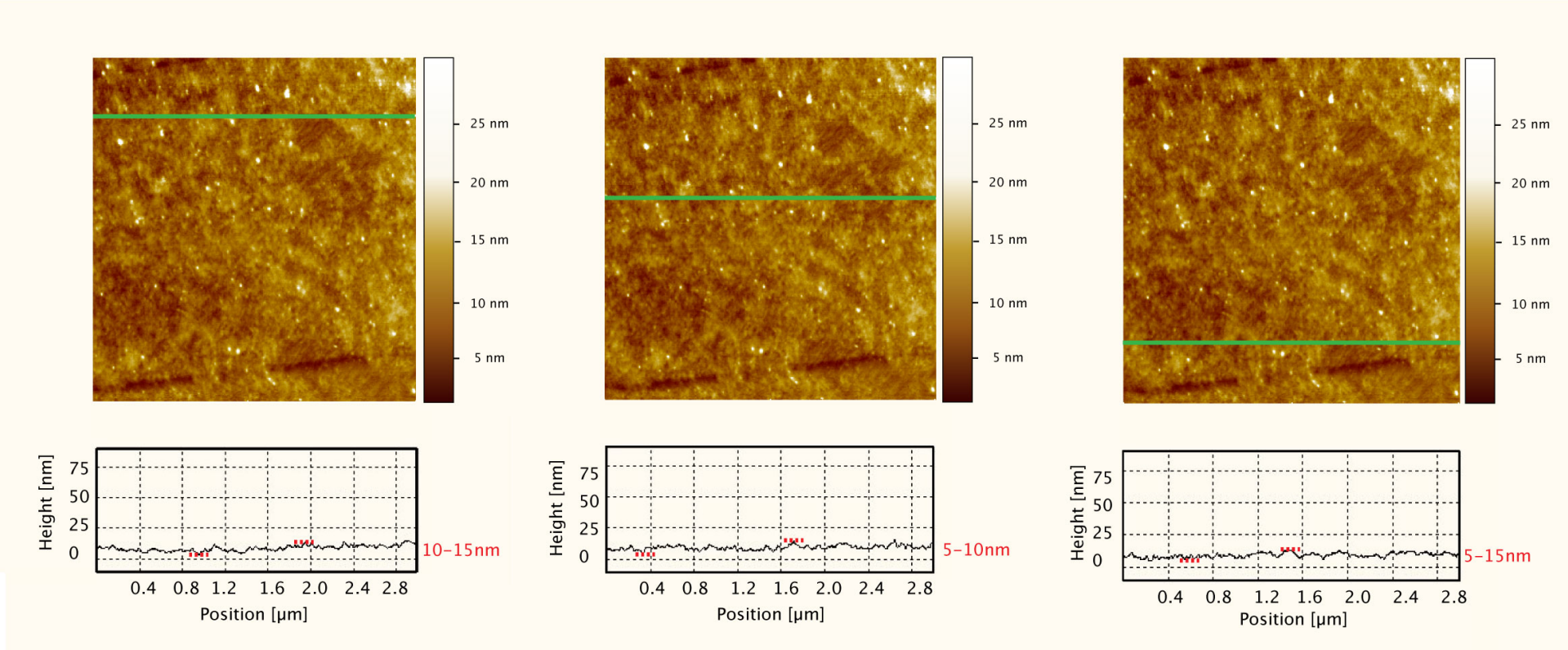

Fig 4.4

AFM images in OD-3 with 1000°C annealing for 1-hour. These images are enlarged 3 μm × 3 μm squares. Green line shows the position of each cross-section, and the profiles are below each topographical image. Values beside each profile are the amplitudes.

Acknowledgement

Prof. Noriko HASEBE who is my supervisor gave a lot of helpful advice to my doctoral thesis. Similarly, Prof. Kenji KASHIWAYA and Prof. Keisuke FUKUSHI also gave the advices for the thesis. Prof. Noritaka ENDO helped with the image processing in the Java programming language. Prof. Atsushi MATSUKI and Prof. Takeshi FUKUMA gave the advices on AFM observations. I would like to express my sincere gratitude for their help.

References

Aitken, M.J., 1990. Science-Based Dating in Archaeology. Long- man, London. 274 pp.

Aitken, M.J., 1998. An Introduction to Optical Dating: The Dating of Quaternary Sediments by the Use of Photon-Stimulated Luminescence. Oxford Univ. Press, Oxford. 267 pp.

Ali, A. and Durrani, S.A., 1977. Etched-track kinetics in isotropic detectors. *Nucl. Track Detect*. 1, 107-121.

Angell, J. K. and Korshover, J., 1985. Surface Temperature Changes Following the Six Major Volcanic Episodes between 1780 and 1980. *Jour. Climate and Appl. Meteor*., **24**, p. 937-951.

Bailey, R.A., Dalrymple, G.B. and Lanphere, M.A., 1976. Volcanism, structure and geochronology of Long Valley Caldera, Mono Country, California. *J. Geophys. Res*., **81**, 725-744.

Berger, G.W., 1992. Dating volcanic ash by use of thermoluminescence. Geology, 20, 11-14.

Berger, G.W. and Huntley, D.J., 1994. Tests for optically stimulated luminescence

from tephar glass. *Quaternary Science Reviews*, **13**, Issues 5 – 7, Pages 509-511.

Bigazzi, G., Ercan, T., Oddone, M., Ozdogan, M. and Yegingil, Z., 1993. Application of fission track dating to archaeometry: Provenance studies of prehistoric obsidian artifacts. *Nucl. Tracks Radiat. Meas.* 22, 757-762.

Bigazzi, G., Bonadonna, F.P., Centamore, E., Leone, G., Mozzi, M., Nisio, S. and Zanchetta, G., 2000. New radiometric dating of volcanic ash layers in Periadriatic foredeep basin system, Italy. Palaeogeog- raphy, Palaeoclimatology, Palaeoecology 155, 327–340.

Black, R.F., 1975. Late-Quaternary geomorphic processes : Effects on the ancient Aleut of Umnak island in the Aleutians. *Arctic*, **28**, 160-169.

Borchardt, G.A., Harward, M.E. and Schmitt, R.A., 1971. Correlation of volcanic ash deposits by activation analysis of glass separates. *Quat. Res.* 1, 247-260.

Bragin, V.Y., Reutsky, V.N., Litasov, K.D., Mal'kovets, V.G., Travin, A.V. and Mitrokhin, D.V., 1999. Paleomagnetism and 40Ar/39Ar-dating of Late Mesozoic Volcanic Pipes of Minusinsk Depression (Russia). Physics and Chemistry of the Earth. Part A 24, 545 – 549.

Brown, N.M.D. and Liu, Z.H., 1996. The etching of natural alpha-recoil tracks in

mica with an argon RF-plasma discharge and their imaging via atomic force microscopy, *Surface Science*, **93**, 89-100.

Carpenter, B.S. and Reimer, G.M., 1974. Calibrated Glass Standards for Fission Track Use. NBS Spec. Pub, p. 260.

Cowan, G.A. and Adler, H.H., 1976. The variability of the natural abundance of ^{235}U. Geochem. Cosmochim. Acta 40, 1487-1490.

Dartyge, E., Duraud, J., P., Langevin, Y. and Maurette, M., 1981 New model of nuclear particle tracks in dielectric minerals, *Physical Review B* **23**, 5213–5229.

Fattahi, M. and Stokes, S., 2003. Dating volcanic and related sediments by luminescence methods: a review, *Earth-Science Reviews*, **62**, 229-264.

Fitzgibbon, A. W. and Fisher, R. B., 1995. *A Buyer's Guide to Conic Fitting*. Proc.5th British Machine Vision Conference, Birmingham, pp. 513-522.

Gentner, W., Storzer, D., and Wagner, G. A., 1969. New fission track ages of tektites and related glasses, *Geochim. Cosmochim. Acta* 33, 1075-1081.

Gleadow, A.J.W., Hurford, A.J. and Quaife, R.D., 1976. Fission track dating of zircon: Improved etching techniques. Earth and Planetary Science Letters, 33, 273-276.

Hanna, G.C., Westcott, C.H., Lemmel, H.D., Leonard, B.R., Story, J.S. and Attree, P.M., 1969. Revision of values for 2200 m s1 neutron constants for four fissile nuclides. Energy Rev. 7 (4), 3-92.

Hasebe, N., Barbarand, J., Jarvis, K., Carter, A. and Hurford, A.J., 2004. Apatite fission- track chronometry using laser ablation ICP-MS. Chem. Geol. 207 (3e4), 135-145.

Hashemi-Nezhad, S., R., 1998, The triangular track contours in phlogopite mica detectors and discontinuity of the etchable damage, *Nuclear Instruments Methods B* **142**, 98-110.

Heiken, G. and Wohletz, K., 1985. Volcanic Ash. Univ. California Press, Berkeley. p. 246.

Hildreth, W., 1981. Gradients in silicic magma chambers: implications for lithospheric magmatism. *J. Geophys. Res.,* **86**, 10153-10192.

Huang, W. H. and Walker, R. M., 1967. Fossil Alpha-Particle Recoil Tracks: A New Method of Age Determination, *Science*, **155**, 1103.

Hurford, A.J. and Green, P.F., 1982. A users' guide to fission track dating calibration. *Earth and Planetary Science Letters* **59,** 343–54.

Hurford, A.J. and Green, P.F., 1983. The zeta age cali- bration of fission-track dating. *Isotope Geoscience* **1,** 285–317.

Hurford, A.J, 1990. Standardization of fission track dating calibration: Recommendation by the Fission Track Working Group of the I.U.G.S. Subcommission on Geochronology. *Chem. Geol.*, **80**, 171-178.

Imai, N., Shimokawa, K., Sakaguchi, K. and Takada, M., 1992. ESR dates and thermal behaviour of Al and Ti centers in quartz for the tephra and welded tuff in Japan. Quaternary Science Reviews 11, 257–265.

Ito K. and Hasebe N., 2011. Fission-track dating of Quaternary volcanic glass by stepwise etching. *Radiation Measurements*, **46**, Issue 2, Pages 176-182.

Iwano, H., Orihashi, Y., Danhara, T., Hirata, T. and Ogasawara M., 2012. Evaluation of fission-track and U–Pb double dating method for identical zircon grains – Using homogeneous zircon grains in Kawamoto Granodiorite in Shimane prefecture, Japan. *Journal of the Geological Society of Japan* **118**, 365–75 (in Japanese with English abstract).

Iwano, H., Orihashi, Y., Hirata, T., Ogasawara, M., Danhara, T., Horie, K., Hasebe, N., Sueoka, S., Tamura, A., Hayasaka, Y., Katsube, A., Ito, H., Tani, K., Kimura,

J., Chang, Q., Kouchi, Y., Haruta, Y. and Yamamoto, K., 2013. An inter-laboratory evaluation of OD-3 zircon for use as asecondary U-Pb dating standard, *Island Arc*, **22**, 382-394.

Izett, G. A., 1981. Volcanic ash beds: recorders of upper Cenozoic silcic pyroclastic volcanism in the western United States. *J. Geophys. Res.,* **86**, 10200-10222.

Izett, G. A., 1982. The Bishop ash bed and some older compositionally similar ash beds in California, Nevada and Utah. *U.S.Geol. Surv., Open File Rept.,* **82-582**.

Izett, G. A., Wilcox, R. E., Powers, H. A. and Desborough, G. A., 1970. The Bishop ash bed, a Pleistocene marker bed in the western United States. *Quat. Res.,* **1**, 121-132.

Johnson, C.E., Benton, E.R., Yasuda, N. and Benton, E.V., 2009. Analysis of short-range tracks and large track fluences in CR-39 PNTD using atomic force microscopy. Radiation Measurements 44, 742-745.

Kaneoka, I., 1972. The effect of hydration on the K/Ar ages of volcanic rocks. Earth and Planetary Science Letters, Volume 14, Issue 2, Pages 216-220.

Kitada, N., Wadatumi, K., Masuda, H. and Nagao, K., 1993. K-Ar age of JAS-G1. Fission Track News Lett. 6, 7-10 (in Japanese).

Kitada, N., Wadatumi, K. and Bigazzi, G., 1994a. ITP-FT age determination of glass age standard JAS-G1. Fission Track News Lett. 7, 5-6 (in Japanese).

Kitada, N., Wadatumi, K., Masumoto, S., Togashi, S. and Matsushita, R., 1994b. The chemical analysis of glass age standard JAS-G1. Fission Track News Lett. 7, 3 (in Japanese).

Laj, C., Szeremeta, N., Kissel, C. and Guillou, H., 2000. Geomagnetic paleointensities at Hawaii between 3.9 and 2.1 Ma: preliminary results. *Earth and Planetary Science Letters* 179, 191–204.

Longerich, H.P., Jackson, S.E. and Gunther, D., 1996. Laser ablation inductively coupled plasma mass spectrometric transient signal data acquisition and analyte concentration calculation. J. Anal. Spectrom. 11, 899-904.

Lowe, D.J., McFadgen, B.G., Higham, T.F.G., Hogg, A.G., Froggatt, P.C. and Nairn, I.A., 1998. Radiocarbon age of the Kaharoa Tephra, a key marker for late-Holocene stratigraphy and archeology in New Zealand. The Holocene 8, 487–495.

McDougall, I. and Harrison, T. M., 1988. Geochronology and Thermochronology by the 40Ar/39Ar Method, Oxford University Press, pp.212.

Miallier, D., Faïn, J., Montret, M., Pilleyre, Th., Sanzelle, S. and Soumana, S., 1991. Properties of the red TL peak of quartz relevant to thermoluminescence dating. *Nuclear Tracks and Radiation Measurements* **18**, 89–94.

Miallier, D., Faïn, J., Sanzelle, S., Pilleyre, Th. Montret, M., Soumana, S. and Falguères, C., 1994. Attempts at dating pumice deposits around 580 ka by use of red TL and ESR of xenolithic quartz inclusions. *Radiation Measurements* **23**, 399–404.

Miller, T., P. and Smith, R., L., 1987. Late Quaternary caldera-forming eruptions in the eastern Aleutian arc, Alaska. Geology, 15, 434-438.

Miller, D.S. and Wagner, G.A., 1981. Fission-track applied to obsidian artifacts from South America using the plateau-annealing and the track-size age-correction techniques. Nucl. Tracks 5, 147-155.

Monnin, M.M., 1980. Visualization of latent damage trails. *Nucl. Instr. Meth.*, **173**, 1-14.

Morishita, T., Ishida, Y., Arai, S. and Shirasaka, M., 2005. Determination of multiple trace element compositions in thin (<30 mm) layers of NIST SRM 614 and 616 using laser ablation-inductively coupled plasma-mass spectrometry

(LA-ICP-MS). Geostand. Geoanal. Res. 29, 107-122.

Moriwaki, H., Westgate, J. A., Sandhu, A. S., Preece, S. J. and Arai, F., 2008. New Glass fission-track ages of Middle Pleistocene tephras on Yakushima Island, southern Japan. *Quaternary International*. Volume 178, Issue 1, Pages 128-137.

Naeser, C.W., Izett, G.A. and Obradovich, J.D., 1980. Fission-track and K-Ar ages of natural glasses, *U.S. Geol. Surv. Bull.* **1489**, 31.

Naeser, C.W., Izett, G.A. and Wilcox, R.E., 1973. Zircon fission- track ages of Pearlette family ash beds in the Meade County, Kansas, Geology 1, 187-189.

Neymark, L.A. and Paces, J.B., 2000. Consequences of slow growth for 230Th/U dating of Quaternary opals, Yucca Mountain, NV, USA. Chemical Geology 164, 143–160.

Ohishi, S., 2012. Observation of radiation damage and dating of zircon by Atomic Force Microscope, MSc thesis, Kanazawa University (in Japanese).

Ohishi, S. and Hasebe, N., 2012. Observations of fission-tracks in zircons by atomic force microscope. *Radiation Measurements*, **47**, Pages 548-556.

Otsu, N., 1979. A Threshold Selection Method from Gray-Level Histograms. IEEE TRANSACTIONS ON SYSTREMS, MAN AND CYBERNETICS, VOL.

SMC-9, NO.1, 62-66.

Pearce, N.J.G., Perkins, W.T., Westgate, J.A., Gorton, M.P., Jackson, S.E., Neal, C.R. and Chenery, S.P., 1997. A Compilation of New and Published Major and Trace Element Data for NIST SRM 610 and NIST SRM 612 Glass Reference Materials. Geostandards Newsletter 21, 115-144.

Schneider, C.A., Rasband, W.S. and Eliceiri, K.W., 2012. NIH Image to ImageJ: 25 years of image analysis. Nature Methods 9, 671-675.

Seitz, M.G., Walker, R.M. and Carpenter, B.S., 1973. Improved methods for measurement of thermal neutron dose by the fission technique, *J. Appl.Phys.* **44**, 510-512.

Seward, D., 1979. Comparison of zircon and glass fission-track ages from tephra horizons, Geology 7, 479-482.

Shane, P., Froggatt, P., Black, T. and Westgate, J., 1995. Chronology of Pliocene and Quaternary bioevents and climatic events from fission-track ages on tephra beds, Wairarapa, New Zealand. Earth Planet. Sci. Lett. 130, Issues 1-4, 141-154.

Smith, R. L., 1979: Ash-flow magmatism. *Geol. Soc. Amer. Spec. Pap.*, **180**, 5-27.

Storzer, D. and Wagner, G.A., 1968. Correction of thermally lowered fission track

ages of tektites. Earth Planet. Sci. Lett. 5, 463-468.

Suzuki, S. and Abe, K., 1985. Topological Structural Analysis of Digitized Binary Images by Border Following. COMPUTER VISION, GRAPHICS, AND IMAGE PROCESSING 30, 32-46.

Wagner, G.A., 1976. Altersbestimmung und urananalyse alter objekte mittels spaltspuruntersuchungen. Accad, Nazion. Linc., Atti. Conv. Linc 11, 503-513.

Wagner, G.A., 1979. Correction and Interpretation of Fission Track Ages, Lectures in Isotope Geology, pp. 170-177.

Wagner, G.A. and Van den haute, P., 1992. Fission-track dating. In: Fission-track Dating Method. Kluwer Academic Publishers, pp. 60-62, p. 285.

Walder, G. and Mark, T.D., 1988. Annealing kinetics of radiation damage in artificial obsidian glass. Nucl. Instrum. Methods Phys. Res. Sect. B. 32, 303-306.

Walter, R.C., 1989. Application and limitation of fission-track geochronology to Quaternary tephras. Quaternary Int. 1, 35-46.

Westgate, J.A., 1989. Isothermal plateau fission-track ages of hydrated glass shards from silicic tephra beds. Earth Planet. Sci. Lett. 95, 226-234.

Wilcox, R.E., 1965. Volcanic-ash chronology. In: Wright, H.E., Frey, D.G. (Eds.),

The Quaternary of the United States. Princeton University Press, New Jersey, pp. 807-816.

Wintle, A.G., 1973. Anomalous fading of thermoluminescence in mineral samples. Nature 245, 143–144.

Wintle, A.G., 1974. Factors determining the thermoluminescence of chronologically significant materials. Unpublished D. Phil. thesis, Oxford University, Oxford.

Yasuda, N., Uchikawa, K., Amemiya, K., Watanave, N., Takahashi, H., Nakazawa, M., Yamamoto, M. and Ogura, K., 2001. Estimation of the latent track size of CR-39 using atomic force microscope. Radiation Measurements 34, 45-49.

Zagorski, D.L., Vilensky, A.I., Kosarev, S.A., Miterev, A.M., Zhdanov, G.S. and Mchedlishvili, B.V., 2003. AFM method for investigation of irradiated polymers. Radiation Measurements 36, 233-237.